Microstructures, geochemistry, and geochronology of mica fish: Review and advances

Bruno V. Ribeiro [a,b,*], Christopher L. Kirkland [a,b], Melanie A. Finch [c], Frederico M. Faleiros [d], Steven M. Reddy [b], William D.A. Rickard [e], Michael I.H. Hartnady [a,b]

[a] Timescales of Mineral Systems Group, School of Earth and Planetary Sciences, Curtin, Australia
[b] School of Earth and Planetary Sciences, Curtin University, Bentley, WA 6102, Australia
[c] Department of Earth and Environmental Sciences, James Cook University, Townsville, Queensland, Australia
[d] Department of Mineralogy and Geotectonics, University of São Paulo, Rua do Lago 562, 05508-900, São Paulo, Brazil
[e] John de Laeter Centre, Curtin University, Perth, Australia

ARTICLE INFO

ABSTRACT

Shear zones are one of the most conspicuous structures in orogenic and rifting settings, accommodating high strain, rock displacement and influencing magma emplacement and fluid flow. Since shear zones may be simultaneously or sequentially affected by multiple processes involving mineral reactions, variations in pressure-temperature conditions, fluid-rock interaction, and diffusion, determining the timing of such structures has been one of the major challenges for modern geochronology. Although low- (up to lower greenschist facies) and high-temperature shear zones (above amphibolite facies) are well-dated through low- and high-closure temperature minerals, medium-temperature shear zones developed within the critical temperature window of ~450–550 °C, in which conventional chronometers such as $^{40}Ar/^{39}Ar$ and Rb–Sr applied to mica fish may or may not record the timing of deformation for multiple reasons (e.g., grain size, cooling rate, mineral composition, fluid activity, deformation, neo- and recrystallization). Here, we review the current knowledge on the evolution of mica fish and the effect of deformation on its chemical and isotopic systems. We evaluate the effect on the widely deployed in situ $^{40}Ar/^{39}Ar$ technique. Furthermore, we demonstrate the potential to assess mica fish evolution applying high-spatial resolution microstructural and chemical mapping techniques such as electron backscatter diffraction (EBSD), time-of-flight secondary ion mass spectrometry (ToF–SIMS) and in situ Rb–Sr via triple quadrupole inductively coupled plasma mass spectrometry (TQ-ICP-MS) to a case study of medium-temperature mylonites from the well-characterized Taxaquara shear zone, SE Brazil. We show that mica fish display complex microstructures with variable strain intensity, commonly with low strain inner cores and high strain edges and along kink planes. Strain shadows in mica fish are commonly characterized by low-strain fine-grained muscovite, suggesting recrystallization coeval with ductile deformation. Despite being intensely deformed, muscovite fish Rb–Sr retain the protolith age (c. 600 Ma), whereas recrystallized fine-grained muscovite yields the timing of deformation (c. 550–540 Ma). Synthetic shear bands cross-cutting coarse-grained muscovite fish induce muscovite recrystallization consistent with their distinct chemistry, with recrystallized muscovite characterized by higher Fe–Mg and lower Na suggesting fluid-assisted recrystallization under lower temperature compared to the muscovite fish host. We propose that these shear bands across mica fish play an important role by accommodating grain size reduction and subsequent deformation, leading to the formation of smaller individual mica fish. Grain size reduction, likely enhanced by dynamic precipitation (i.e., coeval crystal-plastic deformation and dissolution-precipitation creep), appears as the key recrystallization mechanism that allows low strain muscovite in strain shadows and shear bands to record the timing of deformation in medium-temperature shear zones, consistent with qualitative Sr diffusion modelling.

1. Introduction

Mineral fish, lozenge-shaped single crystal porphyroclasts embedded in a recrystallized matrix, are one of the most conspicuous (micro) structures in mylonites. Fish microstructures have been reported also for garnet, leucoxene, quartz, sillimanite, plagioclase, amphibole, pyroxene and olivine (Azor et al., 1997; Bestmann et al., 2004; Ji and Martignole, 1994; Mancktelow, 2002; Oliver and Goodge, 1996; Pennacchioni et al., 2001), yet they are frequently reported in micas, specifically muscovite (Lister and Snoke, 1984; Mukherjee, 2011; ten Grotenhuis et al., 2003). Fish may be employed to determine the kinematics and timing of mylonitization of shear zones (Oriolo et al., 2018; Passchier and Simpson, 1986; ten Grotenhuis et al., 2003). Shear zones are classically defined as high-strain tabular zones that accommodate tectonic strain and associated displacement (Ramsay, 1980), with an important structural control on the movement of fluids within the crust (e.g., aqueous fluids or silicate melts), hence important for metal movement and concentration, and formation of ore deposits (Alsop and Holdsworth, 2004; Carvalho et al., 2016, 2017; Fossen and Cavalcante, 2017; Oriolo et al., 2018; Ramsay, 1980; Ribeiro et al., 2020b; White et al., 1980). Therefore, constraining the timing of ductile deformation (i.e., mylonitization) can be important to elucidate the behaviour of the continental crust in a range of tectonic settings, with implications to economic geology. The timing of low-temperature shear zones developed in the brittle-ductile transition (below greenschist facies) is commonly determined by using low-temperature thermochronometers such as fine-grained illite K–Ar and apatite fission-track and (U–Th)/He (e.g., Glorie et al., 2019; Hueck et al., 2022, 2020; Mora et al., 2013; Wölfler et al., 2010). The timing of deformation of high-temperature shear zones may be determined by high closure temperature minerals crystallized/recrystallized during deformation (e.g., zircon, monazite, titanite; (Carvalho et al., 2017, 2016; Finch et al., 2017; Giraldo et al., 2019; Oriolo et al., 2018, 2016, 2015). Yet, the timing of medium-temperature shear zones is more contentious given the uncertain overlap between deformation temperature and the closure temperature for key thermochronometers, such as micas, which may vary significantly according to the grain size (i.e., diffusion radius), cooling rate, and mineral composition, all of which affect diffusion parameters.

A range of mineral and isotopic systems have been used to constrain the timing of mylonitization, with mica fish being one of the most dated minerals in medium-temperature mylonites (see Oriolo et al., 2018 for a review). Since both biotite and muscovite, dominant micas in crustal rocks, have potassium (K) as a main constituent, they can be dated by K–Ar and $^{40}Ar/^{39}Ar$ due to the ^{40}K radioactive decay to radiogenic ^{40}Ar. In addition, the electronic affinity between K and Rb allows micas to assimilate Rb during crystallization, which opens an alternative possibility to date micas using the Rb–Sr isotopic system (e.g., Freeman et al., 1997; Hickman and Glassley, 1984; Jenkin et al., 1995). The availability of these isotopic systems and the apparently syn-kinematic fish microstructure has led to widespread use of mica fish as analysed by K–Ar, $^{40}Ar-^{39}Ar$, or Rb–Sr to determine the timing of mylonitization or at least to place some temporal constraints on this fabric (Airaghi et al., 2018; Cabrita et al., 2021, 2022; Challandes et al., 2008; Dunlap et al., 1991; Freeman et al., 1997; Gutiérrez-Alonso et al., 2015; Kelley, 1995, 2002; Kirkland et al., 2007; Mulch et al., 2002; Mulch and Cosca, 2004; Reddy et al., 1996, 1997; Warren et al., 2012; Zhu et al., 2005).

Although fabric-forming micaceous microstructures in mylonites are key for revealing the ductile events imprinted in mylonites, the geochronological interpretation is still contentious (Challandes et al., 2008; Jenkin, 1997; Larson et al., 2023; Ribeiro et al., 2023; Warren et al., 2012). While most researchers interpret mica fish ages using the principles of thermochronology, micas in mylonites are prone to deform, recrystallize and to interact with fluids, which highlights the potential of fluid mediated rather than thermally activated volume diffusion processes dominating the recorded isotopic signal. Depending on the degree to which recrystallization affected the isotopic record, it could

invalidate the concept of closure temperature or even closure interval in the sense of Dodson (1973). Despite great advances in understanding the interplay between deformation-recrystallization and isotopic behavior in a range of minerals (Erickson et al., 2015; Fougerouse et al., 2021b; Gordon et al., 2021; Moser et al., 2022; Odlum et al., 2022; Reddy et al., 2007, 2009a; Ribeiro et al., 2020a; Timms et al., 2011), microstructural characterization of biotite and muscovite via high spatial resolution electron backscatter diffraction (EBSD) and microstructurally-controlled chemical and isotopic analysis have been comparatively poorly explored. Recent analytical improvements in EBSD detectors that enhance mica indexing and collision-reaction-cell inductively coupled plasma mass spectrometers (CRC-ICP-MS) that resolve the Rb–Sr isobaric interference (Hogmalm et al., 2017; Zack and Hogmalm, 2016), have opened a new avenue to explore the interplay between mica fish microstructures and in situ chemistry-isotopes in distinct micas textures (Ribeiro et al., 2023).

Here, we review and expand the current knowledge regarding mica fish microstructures, geochemistry, and geochronology in medium-temperature mylonites by applying cutting-edge high-spatial resolution microstructural and chemical mapping via EBSD and time-of-flight secondary ion mass spectrometer (ToF-SIMS). In addition, distinct muscovite fish microstructures were dated via in situ Rb–Sr analysis. For this purpose, we selected a range of mylonites in the medium-temperature Taxaquara shear zone from the Neoproterozoic-Cambrian Ribeira Belt (SE Brazil), which has a well-characterized structural, metamorphic, and chronological evolution (Ribeiro et al., 2019, 2020a, 2020b), providing a key background to support a focused study on mica fish. This contribution builds on the classic knowledge on the evolution of mica fish (after Lister and Snoke, 1984; Mukherjee, 2011; ten Grotenhuis et al., 2003) and the influence of deformation on mica isotopes (Dunlap et al., 1991; Eberlei et al., 2015; Freeman et al., 1997; Glodny et al., 2008, 1998; Jenkin et al., 1995; Kühn et al., 2000; Mulch et al., 2002; Mulch and Cosca, 2004; Reddy et al., 1996; Ribeiro et al., 2023; Von Blanckenburg et al., 1989; among many others).

2. Mica fish: classification and microstructures

Mineral fish are a characteristic (micro)structure in mylonites, which develop in a range of minerals such as micas (especially white micas), tourmaline, K-feldspar, plagioclase, garnet and quartz (Lister and Snoke, 1984; Mukherjee, 2011; Passchier and Trouw, 2005; ten Grotenhuis et al., 2003; Trouw et al., 2010). Here, we focus on the classification and microstructures of mica fish (muscovite and biotite) from medium-to high-temperature mylonites.

The pioneering study by ten Grotenhuis et al. (2003) proposed a mica fish classification based on the shape and orientation of lattice planes after analysing ~1500 muscovite fish from upper-greenschist facies mylonitic quartzites (Fig. 1). Lenticular mica fish (group 1) are characterized by curved sides ending in sharp tips with lattice planes (e.g., cleavage) subparallel to the long axis. Some lenticular fish can deflect into the planes of mylonitic foliation (group 2), leading to curved lattice planes at the tips. Rhomboidal mica fish display straight edges with the longest side parallel to the shearing direction, with lattice planes parallel (group 3) or oblique to shearing (group 4; less common). Mica fish may also display small aspect ratio and smoothly curved shape with no clear relationship between the lattice planes and the long axis (group 5). Elongated thin mica fish have a high aspect ratio and are commonly oriented with their long axis parallel or at a small antithetic or synthetic angle to the mylonitic foliation, sometimes with star stepping shape (group 6; ten Grotenhuis et al., 2003). A further mica fish classification with 11 sub-types is proposed in Mukherjee (2011) based on sheared rocks from the Karakoram Metamorphic Complex only with slight modifications from previous proposal (ten Grotenhuis et al., 2003).

Initial thoughts about the evolution of mica fish relied on brittle deformation, suggesting that they formed in rocks where pre-existing large micas were boundinaged by a combination of brittle and crystal-
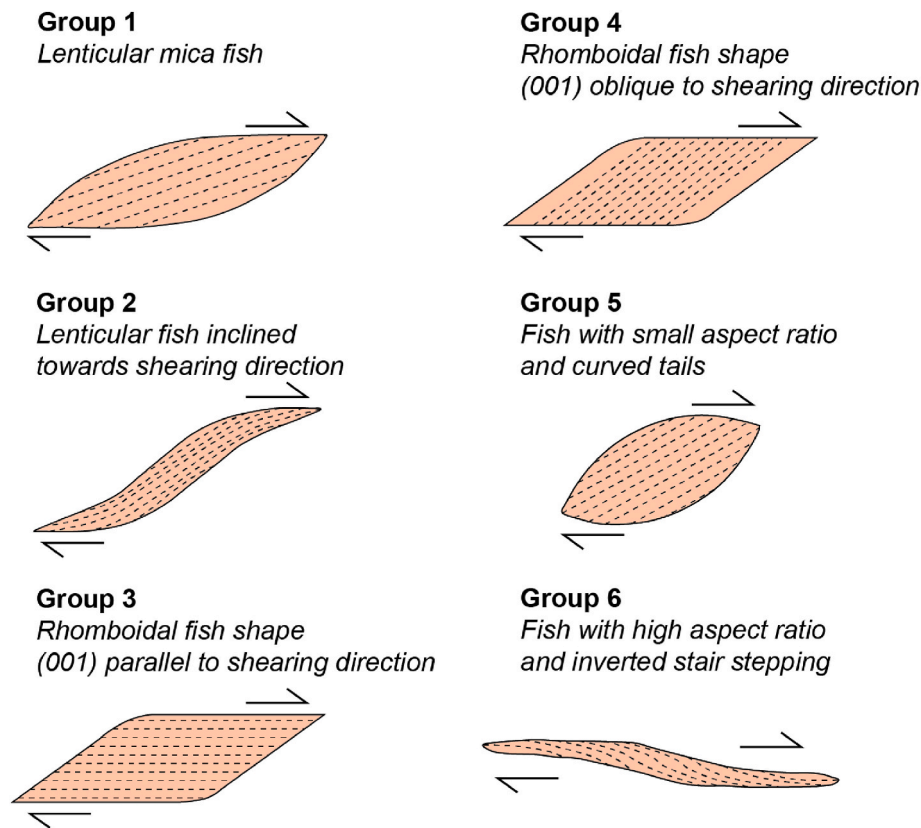
Group 1
Lenticular mica fish

Group 4
Rhomboidal fish shape
(001) oblique to shearing direction

Group 2
Lenticular fish inclined
towards shearing direction

Group 5
Fish with small aspect ratio
and curved tails

Group 3
Rhomboidal fish shape
(001) parallel to shearing direction

Group 6
Fish with high aspect ratio
and inverted stair stepping

Fig. 1. Morphology of mica fish from ten Grotenhuis et al. (2003). Dashed-black lines indicate the typical cleavage orientation of each mica fish group. Black arrows indicate the relative dextral kinematics.

plastic processes, producing asymmetric clasts with (001) cleavage planes sub-parallel to the C-surfaces (shearing planes) or tilted back against the sense of shearing (Heisbacher, 1970; Lister and Snoke, 1984). According to these authors, the segregation of individual mica fish is due to microfaults and microshear zones that transect the host clast (Fig. 2A), which can form synthetically and antithetically depending on the (001) cleavage plane orientation (Lister and Snoke, 1984). Those initial models on the evolution of mica fish provided the grounds for further investigations, which considered a combination of mechanisms including rigid body rotation, crystal-plastic deformation, bending and folding, grain size reduction (recrystallization) and diffusional mass transfer (Mukherjee, 2011; ten Grotenhuis et al., 2003). After evaluating and discussing various generation mechanisms, ten Grotenhuis et al. (2003) suggested that crystal-plastic deformation combined with rigid body rotation were likely key mechanisms in the evolution of mica fish (Fig. 2B). Despite great effort in elucidating the mechanisms of mica fish formation, the roles of crystal-plastic deformation, recrystallization, cataclasis, and diffusional mass transfer have never been assessed by high-spatial resolution techniques, allowing a complete crystallographic and chemical characterization of mica fish and associated microstructures such as shear bands and strain shadows.

3. Dating mica fish

Determining the timing of ductile deformation in shear zones (i.e., mylonitization) has always been a geochronology challenge, particularly because of relic isotopic systems of pre-shearing history, which are variably reset (e.g., Kirkland et al., 2023). Since mylonitization is strongly governed by thermal effects, the timing of shearing is commonly constrained by thermochronology with ages obtained from a range of isotopic systems and minerals, ideally allowing the reconstruction of the thermal pathway for a rock (see Oriolo et al., 2018 for a

review). This approach critically relies on isotope diffusion controlled by thermally-induced volume diffusion and, in such situation, the concept of closure temperature is valid (i.e., whereby the date represents the point in the temperature-time history at which the loss of daughter isotopes from the crystal via diffusion became negligible; Dodson, 1973). However, mylonitization is commonly accompanied by metamorphic reactions, fluid flow and strain partitioning, which may heterogeneously affect the isotopic systems in most datable minerals such as micas, monazite, titanite, apatite and zircon (Cioffi et al., 2019; Dunlap, 1997; Dunlap et al., 1991; Erickson et al., 2015; Fougerouse et al., 2021b; Freeman et al., 1997; Gordon et al., 2021; Kavanagh-Lepage et al., 2022; Kirkland et al., 2017; Kirschner et al., 1996; Kohn, 2018; Moser et al., 2022; Mulch et al., 2002; Odlum et al., 2022; Papapavlou et al., 2017; Reddy et al., 1996, 2007, 2009a; Ribeiro et al., 2020a; Timms et al., 2011; Wawrzenitz et al., 2012; Williams et al., 2011). Here, we focus on the relationship between mica fish microstructures (especially muscovite) and in situ Rb–Sr dating, one of the most datable mineral microstructures in mylonites (Dunlap et al., 1991; Freeman et al., 1997; Mulch et al., 2002; Reddy et al., 1996; Ribeiro et al., 2020b, 2023; Sanchez et al., 2011). For a review about other aspects of geochronology within shear zones, we refer to Oriolo et al. (2018), in which the authors addressed a range of thermal, isotopic, and deformation-related processes relevant to determining the timing of mylonitization in shear zones.

3.1. Isotopic methods

K–Ar, ^{40}Ar/^{39}Ar, and Rb–Sr are the most commonly used isotopic methods for dating mica fish from low-to medium-temperature shear zones (Dunlap et al., 1991; Eberlei et al., 2015; Freeman et al., 1997; Kelley, 2002; Kirschner et al., 1996; Kligfield et al., 1986; Mulch et al., 2002; Reddy et al., 1996; Ribeiro et al., 2020b, 2022b; Van Daele et al.,
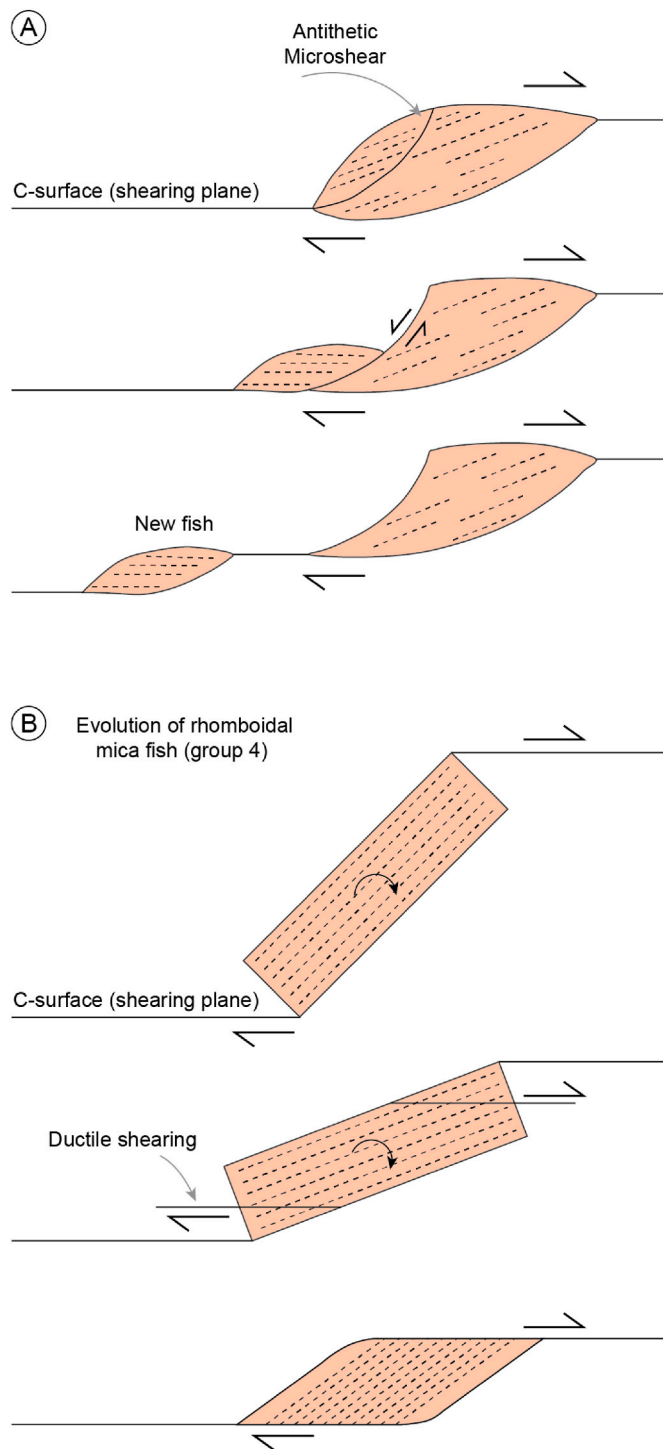
Fig. 2. Schematic evolution of mica fish (adapted from Lister and Snoke, 1984; ten Grotenhuis et al., 2003). A) Model from Lister and Snoke (1984), which initially considered brittle deformation as the main process in the evolution of mica fish; B) Model from ten Grotenhuis et al. (2003) to describe the evolution of rhomboidal mica fish considering rigid body rotation and shearing deformation.

2020). The K–Ar system relies on the radioactive decay of ^{40}K to ^{40}Ar via electron capture followed by γ-ray emission following a ^{40}K decay constant of 0.581×10^{-10} yr^{-1} (Steiger and Jager, 1977). In this method, K isotopes are measured by conventional chemical methods (e.g., isotope dilution and atomic absorption spectroscopy) and Ar isotopes measured by an argon extraction line coupled to a static gas mass spectrometer in separate aliquots (Kelley, 2002). Due to instrument limitations, this method does not allow in situ isotopic measurements, preventing a texturally controlled investigation on the influence of mineral deformation in the K–Ar isotopes.

Although similar to K–Ar, the ^{40}Ar/^{39}Ar isotopic system relies on the conversion of ^{39}K to ^{39}Ar after irradiation of the sample with fast neutrons in a nuclear reaction. The ^{40}Ar/^{39}Ar age is then calculated considering the ^{40}Ar decay and the J-value (a parameter associated with the irradiation process) (Renne et al., 2010). In this method, Ar isotopes can be measured collectively in a single experiment by an incremental stepwise heating approach, either excited by a laser or an oven coupled to a mass spectrometer (e.g., ARGUS instrument, ThermoFisher). Such approaches aim to sequentially release Ar from more tightly bound locations within the sample. Typically, such step heating spectra have some relationship between apparent age, chemistry, microstructure, and mineralogy (and potentially excess ^{40}Ar) within the sample. Furthermore, spatially controlled ^{40}Ar/^{39}Ar analysis is possible by ablation using infrared (IR) of ultraviolet (UV) laser ablation approaches to target specific mineral textures. The in situ UV-laser ablation technique provided the grounds to investigate excess radiogenic ^{40}Ar distribution within a single mineral grain in association with compositional variations (Kelley, 2002, 1995; Nteme et al., 2023; Sherlock and Kelley, 2002) and diffusion of ^{40}Ar excess through the mineral lattice (Kelley, 2002; Reddy et al., 1996, 2001).

Thus, laser ablation approaches using infrared (IR) of ultraviolet (UV) laser allow microstructurally-controlled in situ ^{40}Ar/^{39}Ar analysis with high spatial resolution and spotsize down to 10 μm (Challandes et al., 2003; Chen et al., 2016; Mulch et al., 2002; Reddy et al., 1996; Schneider et al., 2013). For this reason, most of the studies on the influence of deformation on isotopes within mica have relied on the ^{40}Ar/^{39}Ar system, which may not respond in a similar manner to the Rb–Sr system. Since Ar is a gas entrapped in a K-bearing mineral vacancies that can be released during deformation through small fast-diffusion pathways, ^{40}Ar/^{39}Ar might be more easily impacted by deformation compared to Rb and Sr, since the latter occupies a cationic site in micas structure, imposing energetic barriers to be removed from the crystal lattice (Cosca et al., 2011).

The Rb–Sr isotopic system relies on the radioactive decay of ^{87}Rb to radiogenic ^{86}Sr and by emission of β particles and anti-neutrino (Dickin, 2018), with modern ^{87}Rb decay constant calculations of 1.397×10^{-11} yr^{-1} (Villa et al., 2015) and 1.393×10^{-11} yr^{-11} (Nebel et al., 2011). Due to similar mass/charge ratio (m/z), Rb and Sr isotopes cannot be simultaneously measured by conventional mass spectrometers (quadrupole and multicollector ICP-MS), requiring isotope segregation via ion chromatography separation, followed by further Rb and Sr isotopic measurements in different aliquots (García-Ruiz et al., 2008 and references therein). Mica Rb–Sr has been widely used to tentatively constrain the timing of mylonitization in several shear zones worldwide such as, among many other examples, the Entrelor shear zone, Italian Alps (Freeman et al., 1997), Aar Massif shear zones, Swiss Alps (Challandes et al., 2008) and Zanskar shear zone, northwestern Himalaya (Inger, 1998). Despite producing highly precise isotopic measurements, this method prevents microstructurally controlled isotopic analysis, which are necessary to understand such data in deformed minerals such as mica fish in mylonites. In order to overcome this issue, some researchers have performed microstructurally controlled microsampling from thin sections and subsequent Rb–Sr dating of μg-sized aliquots (Müller et al., 2000a, 2000b). However, this may be only applied to coarse-grained microstructures. Thus, microstructures such as shear bands and mica fish tails have been essentially impossible to be effectively analysed.

Recent advances in mass spectrometers, the so-called triple-quadrupole ICP-MS, including the addition of a collision-reaction-cell (CRC) between two quadrupoles, allow the removal of m/z isobaric interferences in response to isotopes reaction with oxidizing gases such as $O_{2(g)}$, $N_2O_{(g)}$, $NH_{3(g)}$ and $SF_{6(g)}$ injected in the CRC (Hogmalm et al., 2017; Moens et al., 2001; Zack and Hogmalm, 2016). The removal of the

Rb–Sr isobaric interference is promoted by the ^{87}Sr oxidation reaction with N_2O producing $^{87}Sr^{16}O^+$ (103 amu, *atomic mass unit*) and $^{86}Sr^{16}O^+$ (102 amu), and with SF_6 producing and $^{87}Sr^{19}F^+$ (106 amu) and $^{86}Sr^{19}F^+$ (107 amu). Since ^{87}Rb is mostly inert under $N_2O_{(g)}$ and $SF_{6(g)}$ atmosphere (very slow conversion reaction), measurements of Rb and Sr isotopes can be done simultaneously due to the Sr mass jump to higher atomic mass units. This novel technique allows microstructurally controlled collection of Rb–Sr isotopes via in situ laser ablation triple-quadrupole ICP-MS with good spatial resolution (spotsize down to 50 μm) and sufficient precision (~1.5% on micas and feldspar; Zack and Hogmalm, 2016). Additionally, it produces reliable and large datasets constraining the timing of ductile deformation on regional scale (Cabrita et al., 2021; Gyomlai et al., 2022; Kirkland et al., 2023; Larson et al., 2023; Liebmann et al., 2022; Olierook et al., 2020; Ribeiro et al., 2022b, 2023; Van Daele et al., 2020; Zametzer et al., 2022), but also revealing the relationship between microstructures and isotope composition (Ribeiro et al., 2023; Tillberg et al., 2020). The in situ Rb–Sr method opens a new avenue to explore the yet poorly understood influence of deformation in isotopic behaviour during mylonitization with sensible textural control.

3.2. Deformation influence on mica isotopes

The general understanding on the influence of deformation in mineral isotopes relies on the isotopic diffusion through fast-diffusion pathways such as dislocation walls, commonly observed in high-spatial resolution EBSD mapping, transmission electron microscopy and atom probe tomography. The preferential loss (or gain) of specific elements in a parent-daughter isotopic pair over time results in measurably different isotopic signatures. This process has been reported for a range of geochronometers such as zircon (Reddy et al., 2007, 2009a, 2009b; Timms et al., 2011), apatite (Odlum et al., 2022; Ribeiro et al., 2020a), monazite (Erickson et al., 2015; Fougerouse et al., 2021b; Wawrzenitz et al., 2012) and feldspar (Reddy et al., 1999, 2001). Isotopic diffusion through crystal-lattice defects may partially or completely reset the mineral clock in response to a certain tectonic-related deformation event. Such resetting process, driven by the ability of fluids and a transport pathway (i.e., mass transfer phenomena), thus records the timing of elemental mobility on the associated microstructures. Therefore, identifying deformation microstructures in minerals from mylonites can prove crucial to link any isotopic record (containing age information) and mylonitization by establishing a direct time-strain link instead of solely assuming thermal activated volume-diffusion as the primary driver as in the sense of thermochronology (Oriolo et al., 2018, 2022; Ribeiro et al., 2023).

The effect of deformation on mica chronometers has been well investigated with in situ $^{40}Ar/^{39}Ar$ experiments allowing to associate isotopic measurements with specific microstructures (Cosca et al., 2011; Hames and Cheney, 1997; Kellett et al., 2016; Mulch et al., 2002; Mulch and Cosca, 2004; Nteme et al., 2023; Reddy et al., 1996, 1997, 2004; Rogowitz et al., 2015). Aside from fluid and solid inclusions, Ar is located in the mineral lattice defects (e.g., vacancies and interstitial) or line defects such as partial or complete dislocations (Cosca et al., 2011). Since micas (biotite and muscovite) often develop lattice defects (dislocations and line defects) in deformed rocks (Bell et al., 1986; Etheridge et al., 1973; Etheridge and Hobbs, 1974; Wilson and Bell, 1979), Ar might diffuse into or out of micas through those microstructural defects. Studies on the $^{40}Ar/^{39}Ar$ isotopic system in micas (biotite and muscovite) carried out with in situ analysis (via infrared and UV laser ablation systems) indicate that mesoscopic and submicroscopic structural defects lead to reduction in the effective diffusion length, favouring intragrain radiogenic ^{40}Ar diffusion and consequent isotopic loss (Cosca et al., 2011; Kellett et al., 2016; Kramar et al., 2001, 2003; Mulch et al., 2002). In experimentally deformed muscovite and biotite, radiogenic ^{40}Ar diffusion through structural defects leads to isotopic loss of up to 16 % in muscovite and 32 % in biotite when measured by in situ UV laser

ablation (Cosca et al., 2011). When looking at in situ $^{40}Ar/^{39}Ar$ dates of a single muscovite fish from a Variscan pegmatite (c. 350 Ma) located in the western Swiss Alpes, Kramar et al. (2001) identified a range of dates spanning 387–115 Ma that were statistically correlated with two crystal directions relative to the shear sense of deformation. Based on one-dimensional diffusion modelling, Kramar et al. (2001) established that apparently younger zones in mica fish represent incipient shear band development, providing a network of fast-diffusion pathways for radiogenic ^{40}Ar diffusion leading to intragrain isotopic loss. Microstructural characterization via high-spatial resolution EBSD mapping was not completed in this study, and would have further elucidated the nature of this relationship.

While there are many Ar studies on deformed micas, very few studies have focused on the Rb–Sr system, mostly due to analytical barriers to conduct in situ measurements (Eberlei et al., 2015; Freeman et al., 1997; Ribeiro et al., 2023). Using a combination of mineral chemistry, high-spatial resolution EBSD mapping and in situ Rb–Sr isotopic analyses, Ribeiro et al. (2023) identified that muscovite fish in a medium-temperature mylonite tend to preserve protolith crystallization ages, whereas muscovite in shear bands recrystallized through dissolution-precipitation creep tend to record the timing of mylonitization. Similar to the Ar studies, Ribeiro et al. (2023) demonstrated the role of deformation and recrystallization mechanisms for resetting isotopic systems, since these processes enhance mica grain size reduction leading to shorter effective diffusion length and facilitate isotopic exchange through crystal-lattice defects. This study demonstrated that a time-gap of ca. 1 Ga between mostly rigid mica fish with little evidence of well-developed crystal-lattice defects and recrystallized fine-grained micas in shear bands, with the latter establishing the direct time-strain evolution of complex mylonites. In this review, we expand the knowledge on mica deformation associated chemical and Rb–Sr isotopic variations.

4. Methods

4.1. Electron microscopy

Mica fish textures were detailed through scanning electron microscopy to collect high-resolution backscatter electron (BSE) images and high-spatial resolution EBSD data. BSE images and EBSD data were collected with a TESCAN Clara field emission scanning electron microscope (coupled to an Oxford Symmetry EBSD detector) at the John de Laeter Centre, Curtin University, Australia. Backscatter electron images were collected in a high-resolution mode using a thin carbon coat to mitigate charging (~2.5 μm thickness), low energy of 10 kV, beam current of 1 nA and working distance of 10 μm.

EBSD analysis were conducted on polished thin sections cut parallel to the kinematic plane (XZ plane in the finite strain ellipsoid). Thin sections were polished on a Buehler VibroMet II for 4 h using a 0.05 μm colloidal silica solution (ethylene glycol-based) prior to data collection. A thin carbon coat was applied to mitigate charging (~2.5 μm thickness). Analytical conditions include 20 keV voltage, 1 nA beam current, 20 mm working distance, 70° sample tilt, 40–50 ms exposure time to enhance indexing and variable step-sizes as indicate in the EBSD maps. EBSD data were processed with AZtecCrystal 2.1 and further colour-formatted using Adobe Illustrator™ and Photoshop™. Monoclinic-hexagonal pseudo-symmetry in muscovite (<-10-3>/120°, 5° angle deviation) was quantified in the inverse pole figure (IPF) maps and removed during post-processing. Details regarding each EBSD maps and associated pole figures are presented in respective figures and captions.

4.2. ToF-SIMS

Mica fish grains with particular microstructures were selected for detailed chemical-isotopic imaging via ToF-SIMS. The analyses were carried out on a M6 instrument (IONTOF GmbH) at the John de Later

Centre, Curtin University, Australia. The instrument was operated in Fast Imaging mode with a 30 kV Bi_1^+ primary ion source at a pulsed current of 0.05 pA. Positive ions were collected using Delayed Extraction mode for the mass analyser at a cycle time of 45 μs. with the analytical conditions resulted in a lateral resolution of ~100 nm and a mass resolution of ~3000 M/ΔM. Maps were collected over a 300 × 300 μm field of view with 2048 × 2048 pixels in each frame. The mass spectra included all masses up to 200 m/z ratio. To remove surface contamination, each field of view was pre-sputtered with a O_2 ion source (2 kV, 479 nA) for 60 s. Surface accumulation of material from degassing/adsorption during the long analyses was removed by sputter cleaning for 1 s after each analysis frame (every 210 s). Data was analysed using IONTOF Surface Lab version 7.3.

4.3. In situ Rb–Sr geochronology

In situ Rb–Sr isotopes were collected in polished thin sections in the GeoHistory Facility, Curtin University. The analytical setup includes a RESOlution 193 nm ArF excimer laser with a Laurin Technic S155 sample cell coupled to an Agilent 8900 triple quadrupole mass spectrometer in MS/MS mode using the $N_2O_{(g)}$ as reaction gas in the collision cell to enable measurement of Rb and Sr isotopes (Cheng et al., 2008; Hogmalm et al., 2017; Zack and Hogmalm, 2016). The analytical conditions for Rb–Sr are summarized in Table 1 following the method described elsewhere (Liebmann et al., 2022; Olierook et al., 2020; Ribeiro et al., 2023). Data reduction was performed in Iolite 4 (Paton et al., 2011) using an in-house data reduction scheme adapted from Redaa et al. (2021). Rb–Sr isochrons and ages were calculated using the maximum likelihood model in IsoplotR (Vermeesch, 2018) with the ^{87}Rb decay constant of Villa et al. (2015). Ages and uncertainties are presented at 2 standard error from the mean (2 SE), with error propagation and error correlation following Rösel and Zack (2022). Inverse Rb–Sr isochrons are used to minimize the extreme error correlation following Li and Vermeesch (2021). Rb–Sr isotopic dataset from reference materials and unknowns are presented in supplementary material S1.

$^{87}Sr/^{86}Sr$ and $^{87}Rb/^{86}Sr$ ratios were drift-corrected and calibrated against NIST610 ($^{87}Sr/^{86}Sr = 0.709699 \pm 0.000018$, $^{87}Rb/^{86}Sr = 2.389 \pm 0.005$; Woodhead and Hergt, 2001). Matrix correction of drift-corrected $^{87}Rb/^{86}Sr$ was applied to mica analyses using a fractionation factor obtained from a pressed powder tablet of phlogopite Mica-Mg that was analysed interspersed with the unknowns, assuming a crystallization age of 519.4 ± 6.5 Ma and $^{87}Sr/^{86}Sr_0$ of 0.72607 ± 0.00070 (as described by Hogmalm et al., 2017). Mica-Mg isotopic data yielded an anchored-isochron date of 515 ± 3 Ma (MSWD = 0.7, N = 26), consistent with reference values. Unknowns were additionally bracketed with in-house biotite reference material CK001 (422 ± 6 Ma; Kirkland et al., 2007), which yielded an isochron age of 413 ± 7 Ma (MSWD = 0.2, N = 25).

Table 1
Analytical conditions for acquisition of Rb–Sr isotopes in muscovite.

Settings	Agilent 8900 ICP-MS
	In situ Rb–Sr
Laser system	ASI RESOlution
Wavelength (nm)	193
Repetition rate (Hz)	5
Laser fluency (J.cm^{-2})	2.5
Ablation time (s)	60
Spot size (μm)	64
He flux rate (ml.min^{-1})	320
He carrier gas (l.min^{-1})	0.32
Ar carrier gas (l.min^{-1})	1.0
N_2 addition (ml.min^{-1})	1.2
Reaction gas (collision cell)	30% N_2O in He

5. Case study

5.1. Geological background

We selected three medium-temperature mica fish-bearing mylonites from the crustal-scale Taxaquara shear zone from the Neoproterozoic-Cambrian Ribeira Belt, SE Brazil (Fig. 3a). This belt is commonly interpreted as a NE-trending collisional orogen that formed in response to the convergence between the São Francisco, Paranapanema, Congo, Luís Alves and Rio de la Plata cratons during West Gondwana assembly (Cabrita et al., 2021; Campanha et al., 2023; Campanha and Sadowski, 1999; Campos Neto, 2000; Caxito et al., 2022; Faleiros et al., 2011; Heilbron et al., 2020; Ribeiro et al., 2022a), although alternative intracontinental models have also been proposed (Meira et al., 2015, 2019). The Ribeira Belt comprises a series of terranes including the Apiaí, São Roque, Embu, Costeiro and Curitiba terranes, that are dissected by a major crustal-scale shear zone system developed under transpression between 900 and 530 Ma (Cabrita et al., 2022; Campanha et al., 2023; Campanha and Brito Neves, 2004; Conte et al., 2020; Egydio-Silva et al., 2002, 2005, 2018; Faleiros et al., 2022; Forero-Ortega et al., 2020; Ribeiro et al., 2019, 2020b).

The Taxaquara shear zone (TSZ) is a major dextral NE-striking shear zone that structurally separates the NE-striking Statherian (c. 1750 Ma) São Roque Group, located in the northernmost section of the TSZ, from the NW-striking Calymmian (1490–1475 Ma) Votuverava Group and the Ediacaran (615–585 Ma) Pilar do Sul granitic suites located southern of the TSZ (Fig. 3b). Ductile deformation conditions in the TSZ achieved 480–530 °C and 2.2–5.0 kbar, based on phase-equilibria modelling coupled with mineral chemistry and thermometry (Ribeiro et al., 2019, 2020a). At these conditions and under average 10^{-13}–10^{-12} s^{-1} strain rates, quartz recrystallized through subgrain rotation with preferential activation of 'basal-<a>' and 'rhomb-<a>' slip systems (Ribeiro et al., 2019, 2020a). Muscovite fish $^{40}Ar/^{39}Ar$ and apatite U–Pb dates from mylonites bracket the activation of the TSZ at c. 560–535 Ma (Ribeiro et al., 2020b), coeval with the main shearing deformation of the Ribeira Belt and African counterpart belts during West Gondwana assembly (Faleiros et al., 2022; Goscombe et al., 2005; Gray et al., 2006; Schmitt et al., 2023).

5.2. Medium-temperature mylonites

The selected samples from the TSZ vary from granitic mylonite ultramylonite-phyllonite with variable content of micas (including mica fish and fine-grained mica in the mylonitic matrix) (Table 2). The ultramylonite (sample TG01) is primarily composed of fine-grained Qz + Fsp (90 vol. %) with fine-grained muscovite in the mylonitic matrix and muscovite fish comprising ~10 vol %. Samples PS40A and PS40D were collected in the same quarry, but present distinct mineralogy and microstructures. The former is composed of Qz + Pl + Afs + Bt + Ms, and apatite, rutile and oxides as accessory phases, and displays a fine-grained granolepidoblastic mylonitic texture defined by recrystallized Qz + Fsp matrix accompanied by fine-grained biotite with very few porphyroclasts in addition to muscovite fish (up to 30 vol. %). Although with similar mineralogy, sample PS40D displays garnet and tourmaline as additional accessory phases and coarse-grained Qz + Fsp aggregates with granoblastic textures and abundant large feldspar and muscovite fish porphyroclasts (up to ~10 vol. %). For detailed description of the mylonites from the TSZ, we refer to Ribeiro et al. (2019).

5.2.1. Microstructures

Muscovite fish grains from the mylonitic granite (sample PS40D) display complex microstructures. They show common muscovite fish shapes (e.g., group 1 from ten Grotenhuis et al., 2003) with kink bands and tails composed of fine-grained muscovite (Fig. 4A). In domains with high mica fish connectivity, the grains are more elongated with kink bands sub-perpendicular to the cleavage planes (Fig. 4B). Additionally, a
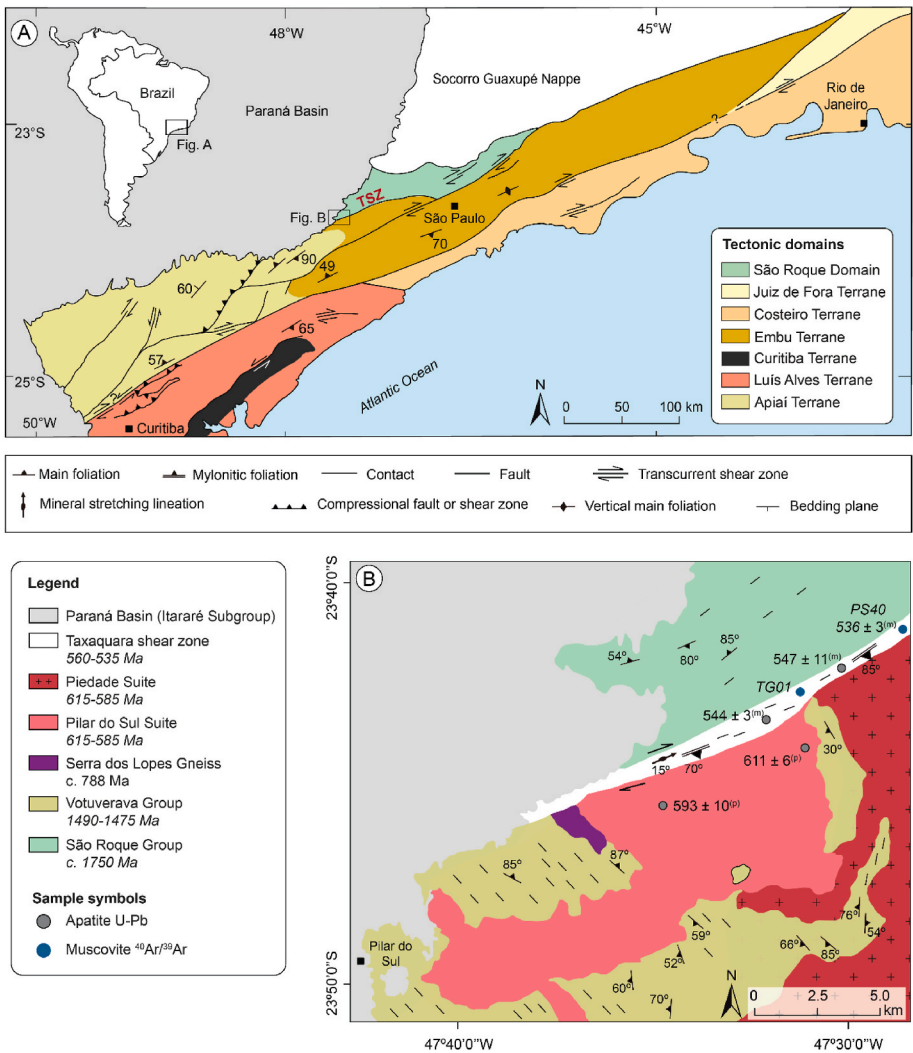
Fig. 3. A) Regional geological setting of the Ribeira belt, tectonic terranes and associated shear zones (adapted from Cabrita et al., 2022); B) Simplified geological map of the study (adapted from Ribeiro et al., 2019). Grey and blue circles indicate apatite U–Pb and muscovite ^{40}Ar/^{39}Ar dates from unde-formed protolith (p) and mylonitic rocks (m) (Ribeiro et al., 2020b). (For interpretation of the references to colour in this figure legend, the reader is referred to the Web version of this article.)

Table 2

Summary of the selected samples for this study, including mineral assemblage, quartz and feldspar microstructures reported in Ribeiro et al. (2019)[1] and previous muscovite fish ^{40}Ar/^{39}Ar dates reported in Ribeiro et al. (2020b)[2]. Mineral abbreviations follow Whitney and Evans (2010).

| Sample	Mineral assemblage[1]	Deformation mechanism[1]		Published geochronology[2]	
		Quartz	Feldspar	^{40}Ar/^{39}Ar date (Ma)	^{40}Ar/^{39}Ar date type
TG01	Qz, Pl, Afs, Ms	Subgrain rotation	Fracture + intracrystalline deformation	549 ± 1 (Ms)*	Total fusion
PS40A	Qz, Pl, Afs, Bt, Ms (±Op, Ap, Rt)	Subgrain rotation	Fracture + intracrystalline deformation	536 ± 3 (Ms)	Plateau
PS40D	Qz, Pl, Afs, Ms (±Grt, Ap, Rt, Tur)	Subgrain rotation	Fracture + intracrystalline deformation	541 ± 2 (Ms)*	Total fusion

microstructural domain composed of fine-grained elongated muscovite oriented parallel to the mylonitic foliation define the boundary between the feldspar porphyroclast and the high-interconnectivity muscovite fish domain (Fig. 4B). One large muscovite fish displays microstructures suggestive of boudinage, splitting into two fish with a low-pressure domain (interboudin) filled with fine-grained muscovite (Fig. 4C). The larger muscovite fish is enveloped by mostly elongated fine-grained muscovite, developing an asymmetrical tail oriented parallel to the mylonitic foliation. (Fig. 4D).

In the quartzofeldspathic ultramylonite (sample TG01), muscovite fish grains display simpler microstructures such as undulose extinction, rarer fine-grained muscovite tails, and grain-scale cracking at high-angles to cleavage planes (Fig. 5A). Muscovite fish from sample PS40A displays a series of microstructures including bent cleavage planes, segregation planes between distinct muscovite fish domains (Fig. 5B),

grain-scale cracking at high-angle to cleavage planes, and fine-grained margins and tails in most muscovite fish textures. A coarse-grained muscovite fish also displays synthetic concave-shape shear bands high-lighted by muscovite with multiple kink and deformation planes (Fig. 5C and D), indicating a domain of localised deformation cross-cutting the host muscovite fish. High-resolution backscatter electron (BSE) images indicate that the highly deformed shear band (Fig. 5D) is bounded by fine-grained elongated muscovite sub-perpendicular to muscovite fish (001) cleavage (Fig. 5E), which is also present in the muscovite fish tails delimiting it from the mylonitic matrix (Fig. 5F). These tails also encompass muscovite grains with mostly random shape preferred orientation and commonly associated with biotite patches.

5.2.2. EBSD

Selected muscovite fish grains with distinct microstructures from
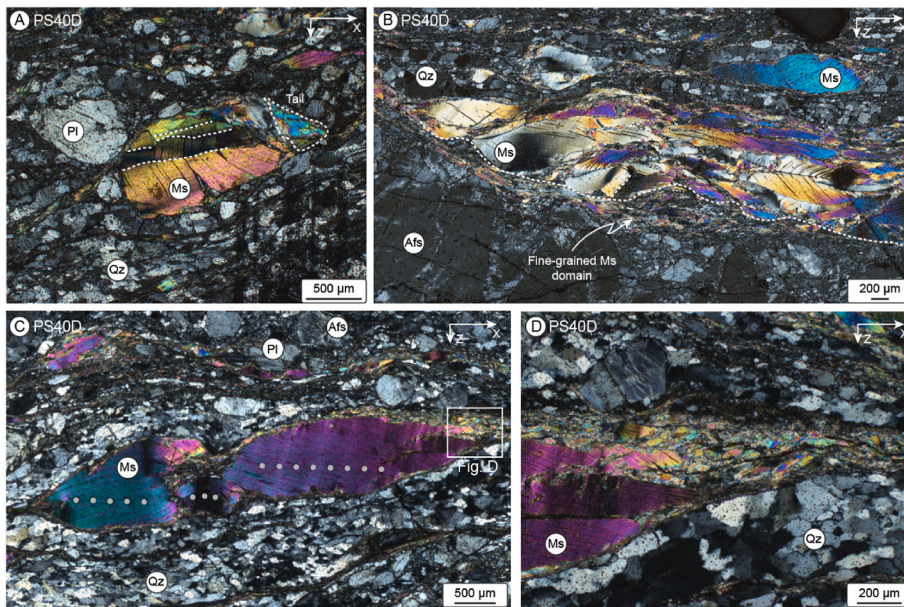
Fig. 4. Muscovite fish microstructures from medium-temperature mylonite from the TSZ. Photomicrographs were undertaken under cross-polarized light. Mineral abbreviations follow Whitney and Evans (2010). Grey circles in © indicate laser spots from in situ Rb–Sr analysis. White dashed-line in (A) indicate kink planes, and in (B) it bounds the muscovite fish aggregates from the fine-grained muscovite domain. Muscovite fish from panel (A) was selected for high-spatial resolution EBSD and in situ Rb–Sr isotopic analysis.

samples PS40A and PS40D were used in high spatial resolution EBSD mapping. From sample PS40D, we selected one asymmetric muscovite fish with kink bands and tails composed of fine-grained muscovite (see Fig. 4A). From sample PS40A, we mapped one asymmetrical muscovite fish with fine-grained muscovite along the grain boundaries and one coarse-grained muscovite fish with oblique shear bands cross-cutting the grain (see Fig. 5C and D).

In the kinked muscovite fish from sample PS40D, we observe higher grain reference orientation deviation-angle (GROD, proxy for strain quantification using EBSD data; Wright et al., 2016) values towards the edges of the grain and along the kink planes that cross-cut the muscovite fish parallel to its maximum elongation (Fig. 6A). The high GROD values suggest a high density of dislocations due to crystal-plastic deformation (i.e., high strain), resulting in a crystallographic spread as indicated by the pole figures for <001> axis. On the other hand, fine-grained muscovite in the tail and surrounding the muscovite fish has low GROD values (suggestive of low strain) accompanied by an asymmetrical girdle-type CPO concordant with <100> sub-parallel to the mylonitic foliation (plane X–Y) and asymmetrical distribution of <001> axis between X–Z directions with higher concentration along the diagram periphery (Fig. 6B). The <001> axis distribution suggests a dextral kinematics consistent with field and petrographic observations (asymmetric feldspar porphyroclasts; Ribeiro et al., 2019).

The asymmetric muscovite fish from sample PS40A displays large GROD variation, increasing from the inner core towards the margins of the grain in all directions (Fig. 7A) and suggesting variation from lower to higher strain density due to higher amount of crystal-plastic deformation along the edges of the grain. Despite this relative strain variation, the muscovite fish presents a strong point-type CPO with <001> maxima in intermediate angle between X–Z directions (Fig. 7B). In contrary, fine-grained muscovite grains along the muscovite fish boundaries have lower GROD values (i.e., low internal strain) accompanied by an asymmetrical girdle-type CPO concordant with dextral kinematics with higher concentration of <001> along the diagram periphery between X–Z directions (Fig. 7B).

In addition to the higher crystallographic misorientation and strain towards the edges and the tips of the muscovite grain from sample PS40A, another coarse-grained muscovite fish from this sample also displays complex microstructures such as synthetic concave-shape structures (shear bands) that cross-cut the fish sub-perpendicular to the cleavage planes. The textural component map indicates that these

shear bands delimit the host fish and fine-grained muscovite with distinct orientation in comparison to the host (Fig. 8A). The GROD map indicates that some of these shear bands are characterized by low strain fine-grained muscovite (Fig. 8B and C), suggesting low internal energy likely due to recrystallization, whereas others display high strain likely due to a higher amount of crystal-plastic deformation prior to achieving complete recrystallization (Fig. 8B, D). As previously indicated through high-resolution BSE images (Fig. 5F), we note the presence of finer muscovite grains in the edges of the fish characterized by high crystallographic misorientation compared to the host fish, but with low GROD values suggestive of low-strain.

5.2.3. ToF-SIMS mapping

ToF-SIMS ion mapping was carried out on the low- and high-strain shear bands of a coarse-grained muscovite fish from sample PS40A to assess the potential relationship between mineral chemistry, deformation intensity and recrystallization mechanisms (see selected areas indicated in Fig. 8A). A detailed EBSD map from the low-strain shear band (area 1) indicate a clear distinction in maximum orientation spread between the fine-grained muscovite in the shear band and the host muscovite fish (up to 34°, Fig. 9A). Since orientation spread acts as a measure of intragranular lattice distortion and a proxy for dislocation density (Cross et al., 2017), the fine-grained muscovite is inferred as mostly strain-free, yet is embedded within a muscovite fish that is crystallographically deformed. ToF-SIMS ion mapping revealed that those low-strain fine-grained muscovite regions have higher Fe–Mg–Ba contents and lower Na. This geochemical difference delimits a sharp compositional boundary between the low-strain shear band and the host fish (Fig. 9B). High Fe–Mg grains correspond to biotite intergrowth within the shear band.

Conversely, a detailed EBSD map from the high-strain shear band (area 2) indicate that both host muscovite fish and the shear band are characterized by high maximum orientation spread up to 66°, suggestive of high intragranular distortion and dislocation density. Yet, the fine-grained muscovite bounding the high-strain shear band previously observed through high-resolution BSE images (Fig. 5E) displayed low orientation spread, suggestive of low strain likely achieved through recrystallization. The ToF-SIMS ion maps of these regions do not indicate a clear compositional variation between the high-strain shear band and the host muscovite fish (Fig. 9B). Yet, the low-strain fine-grained muscovite aligned parallel to the microstructural boundary is enriched
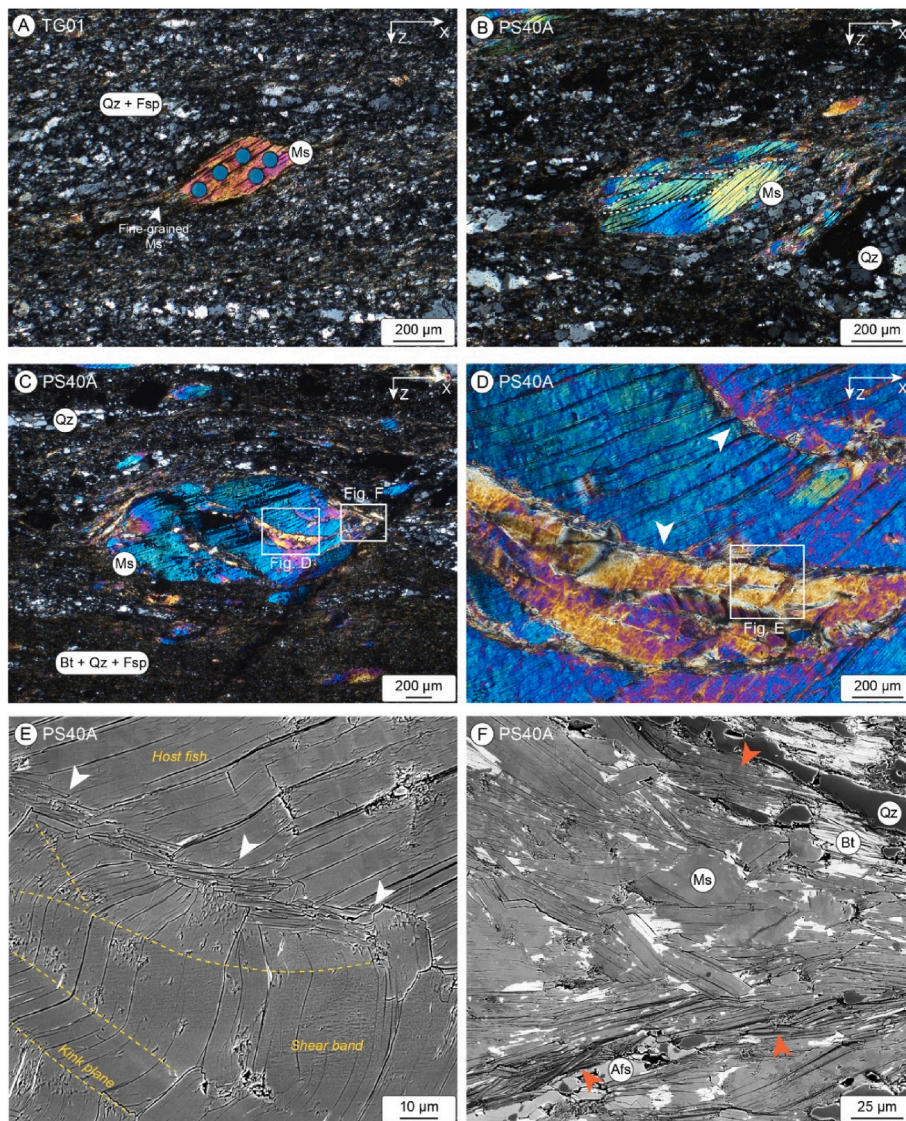
Fig. 5. Muscovite fish microstructures from medium-temperature ultramylonite samples from the TSZ. Photomicrographs were undertaken under cross-polarized light. Mineral abbreviations follow Whitney and Evans (2010). Blue circles in (F) indicate laser spots from in situ Rb–Sr analysis. White dashed-line in (B) indicates segregation planes between distinct muscovite fish 'sub-domains'. Muscovite fish from panel (C) was selected for high-spatial resolution EBSD and in situ Rb–Sr isotopic analysis. (For interpretation of the references to colour in this figure legend, the reader is referred to the Web version of this article.)
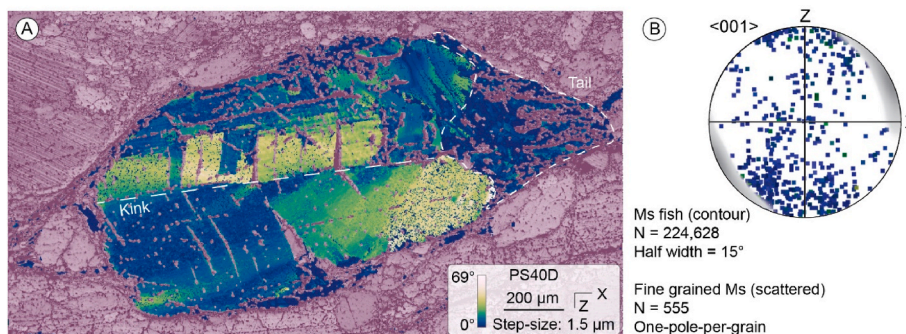
Fig. 6. A) Grain reference orientation deviation angle (GROD) maps of muscovite fish from sample PS40D produced from EBSD data. B) Pole figures were calculated using one-point-per-pixel for single muscovite fish grain (contoured data), and one-point-per-grain for fine-grained muscovite surrounding the muscovite fish (blue squares). Poles figures are presented in lower hemisphere with equal area projection. The muscovite fish crystallographic data is contoured with 15° half width. (For interpretation of the references to colour in this figure legend, the reader is referred to the Web version of this article.)

in Fe–Mg and depleted in Na, similar to those low-strain muscovite grains, defining a sharp chemical boundary between the high-stain shear band and the host muscovite fish.

5.2.4. In situ Rb–Sr geochronology

We targeted distinct muscovite textures during Rb–Sr analysis such as muscovite fish and fine-grained muscovite in asymmetric tails and shear bands. We collected 49 Rb–Sr measurements in muscovite fish from sample PS40A, which yield an inverse isochron date of 592 ± 26 Ma (MSWD = 1.8; Fig. 10A). From sample TG01, we collected 53 Rb–Sr measurements in muscovite fish yielding an inverse isochron date of 588 ± 4 Ma (MSWD = 2.3; Fig. 10B). Asymmetrical tails with fine-grained muscovite from samples PS40A and TG01 are too narrow to be analysed via in situ Rb–Sr.

The granitic mylonite sample PS40D displays muscovite fish surrounded by tails composed by fine-grained muscovite and fine-grained
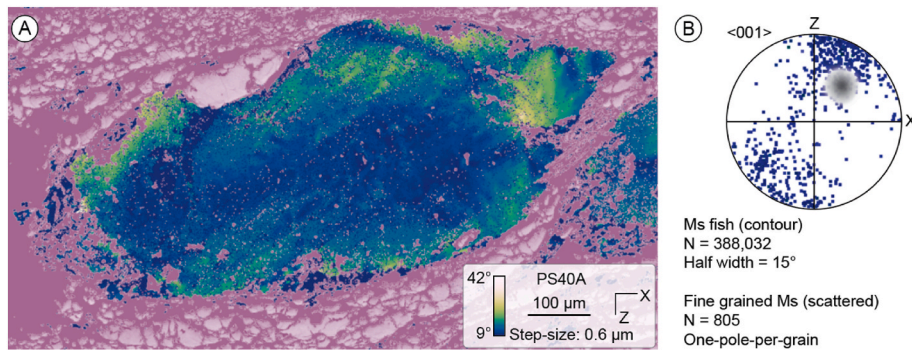
Fig. 7. A) Grain reference orientation deviation angle (GROD) maps of muscovite fish from sample PS40A produced from EBSD data. Sample labels, colour scales and step-size are indicated in each panel (lower right corner); B) Pole figures were calculated using one-point-per-pixel for single muscovite fish grain (contoured data), and one-point-per-grain for fine-grained muscovite surrounding the muscovite fish (blue squares). Poles figures are presented in lower hemisphere with equal area projection. The muscovite fish crystallographic data is contoured with 15° half width. (For interpretation of the references to colour in this figure legend, the reader is referred to the Web version of this article.)
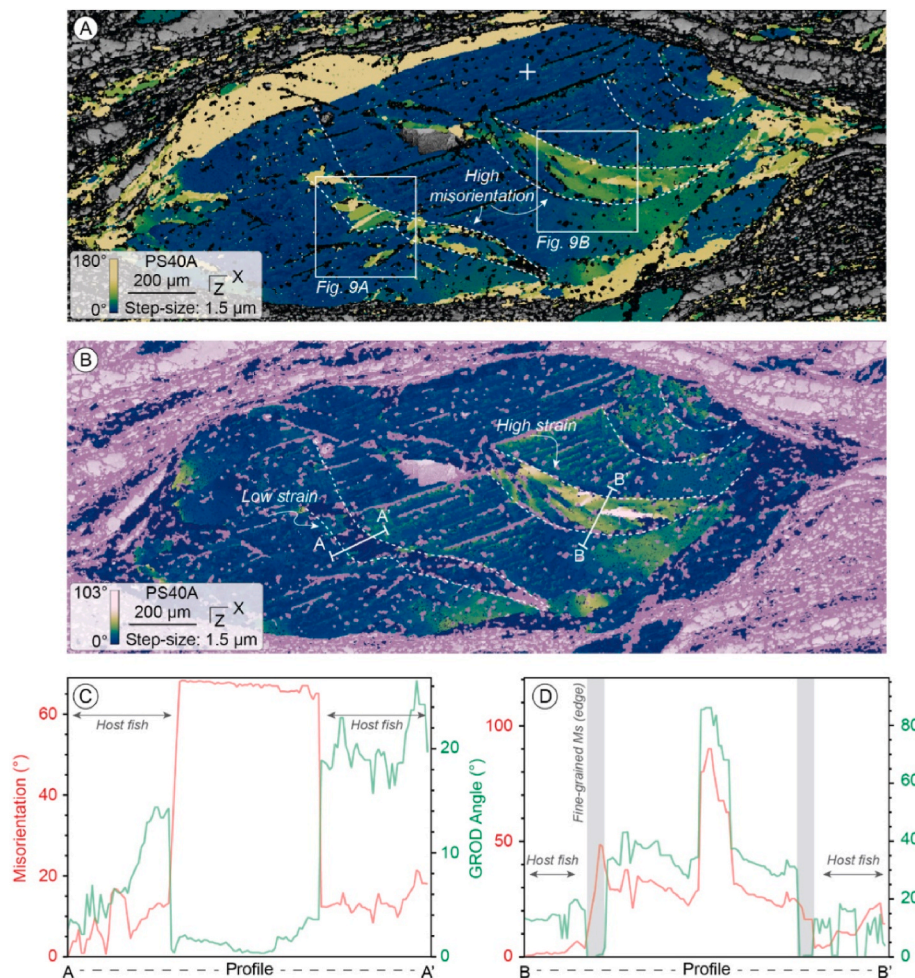

Fig. 8. Textural component (A; relative to the white cross) and grain reference orientation deviation angle (GROD) maps of muscovite fish from sample PS40A produced from EBSD data. C, D) Misorientation and GROD profiles across the shear bands thar cross-cut the muscovite fish (each profile is indicated in panel B). Sample labels, colour scales and step-size are indicated in each panel (lower right corner). Dashed-white lines indicate boundaries between distinct microstructures within the muscovite fish. White rectangles in panel (A) indicate the areas selected for ToF-SIMS ion mapping. (For interpretation of the references to colour in this figure legend, the reader is referred to the Web version of this article.)

muscovite bands. We collected 95 Rb–Sr measurements in muscovite fish, yielding an inverse isochron date of 603 ± 2 Ma (MSWD = 2.5) with 15 analyses being overdispersed from the isochron trend (Fig. 10C). We also collected 23 Rb–Sr measurements in fine-grained muscovite domains, which yielded a younger inverse isochron date of 546 ± 6 Ma (MSWD = 2.4; Fig. 10C). The omitted overdispersed Rb–Sr data were collected in domains with complex microstructural overlap (i.e., coarse- and fine-grained muscovite; see Fig. 4B), in which relict and recrystallized grains coexist. The overdispersed data may represent a mix between the two generations of muscovite or partial resetting due to recrystallization.

6. Discussion

6.1. Forming and deforming mica fish

The early ideas from Heisbacher (1970) and Lister and Snoke (1984) suggested that mica fish formed in rocks where pre-existing large micas were boundinaged by a combination of brittle and crystal-plastic processes, leading to mica fish segregation due to microfaults and microshear that transected the host clast. Further studies suggested that crystal-plastic deformation combined with rigid body rotation were likely the key mechanisms in the evolution of mica fish (Mukherjee, 2011; ten Grotenhuis et al., 2003). Nonetheless, a lack of detailed high-resolution microstructural information has hindered
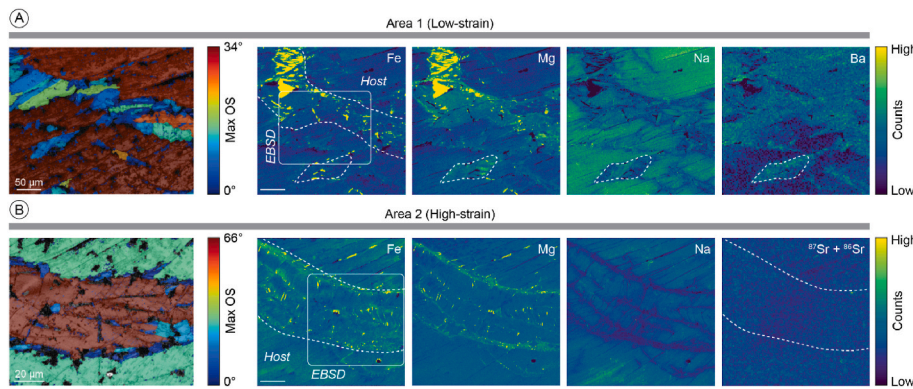
Fig. 9. High-spatial resolution EBSD and ToF-SIMS maps from shear bands cross-cutting a coarse-grained muscovite fish from sample PS40A (see Fig. 8 for reference). A) Maximum orientation spread (based on EBSD data) and Fe–Mg–Na–Ba ion maps from the low-strain domain; B) maximum orientation spread (Max OS), Fe–Mg–Na ion maps and combined Sr isotopes (i.e., sum of ^{87}Sr and ^{86}Sr ion counts) from the high-strain domain. The white scale bar in the ToF-SIMS maps is equivalent to 50 μm. EBSD data were collected using a step-size of 0.4 μm and 0.5 μm (high-strain) shear band.

understanding of this classic microstructure in mylonites.

High-spatial resolution EBSD maps from distinct muscovite fish indicate a high deformation intensity towards the edge of the grain, likely due to simple shearing deformation around a mostly undeformed core as envisaged by Mukherjee (2011), contrasting with previous interpretations that suggested mica fish formation mainly through body rigid rotation (ten Grotenhuis et al., 2003). Here, the effect of simple shear is inferred to be responsible for developing the lozenge fish geometry similar to those patterns obtained from crystal plasticity finite element modelling (Sheikh et al., 2016). In this sense, pre-kinematic muscovite would likely undergo plastic deformation similar to any other porphyroclast in response to the competence difference between the porphyroclasts and the matrix (commonly quartzofeldspathic in crustal mylonites; Platt, 2015). Our observations suggest that the high strain accumulated along the mica fish edges (i.e., intragrain and in the grain-matrix boundary) enhances the development of fine-grained muscovite (Fig. 4A–D, 5B, C, F) which commonly displays low strain and has mostly well-defined synthetic asymmetrical <c>-axis single girdles. These features imply recrystallization coeval with ductile deformation/mylonitization in a process similar to σ-porphyroclasts development (Passchier and Simpson, 1986). As previously demonstrated in Passchier and Simpson (1986), recrystallized material continuously flows away from the porphyroclast which becomes appended by the production of new grains and forms wedge-shaped σ-type tails at high recrystallization/deformation rates, which seems to be the case for the development of mica fish geometries.

Despite being highly strained in some cases, mica fish tend to accommodate deformation through low-angle basal slip in all investigated textures (Fig. 11), similar to what has been demonstrated in deformation analysis studies (Bell et al., 1986; Bell and Wilson, 1981; Mares and Kronenberg, 1993; Meike, 1989; Wilson and Bell, 1979). The lack of activation of multiple slip systems prevents the development of microstructures such as subgrain boundaries like in minerals with complex slip systems such as quartz and feldspar (Dell'angelo and Tullis, 1989; Prior and Wheeler, 1999; Schmid and Casey, 1986; Stipp et al., 2002; Viegas et al., 2016). This structural mica characteristic greatly affects the geochronology of mica fish, given that subgrain development is one of the most efficient ways to mobilise trace elements and isotopes through the establishment of fast-diffusion pathways (Erickson et al., 2015; Fougerouse et al., 2021a, 2021b; Reddy et al., 2007, 2020; Verberne et al., 2022).

6.2. Chemical-strain relationship

Since individual mica fish represents a snapshot of the microstructural evolution during mylonitization, it is rare to identify and characterize the processes that lead to the segregation of new fish grains out of primary coarse-grained mica fish. One coarse-grained muscovite fish from sample PS40A displays exceptional microstructures (Fig. 5C–E)

that might shed light on the mechanisms of mica fish segregation.

Based on detailed high-spatial resolution EBSD and ToF-SIMS ion maps, we know that recrystallized muscovite grains are associated with higher Fe–Mg–Ba and lower Na contents compared to the host muscovite fish, defining clear chemical boundaries between the host and the shear bands and indicating that recrystallization was accompanied by chemical modification. In addition, these low-strain fine-grained muscovite associated with shear bands and fish tails commonly display synthetic asymmetrical <c>-axis single girdles, which is commonly attributed to crystal-plastic deformation (see examples in Ribeiro et al., 2023). Yet, the low-strain characteristics associated with chemical modification suggest that reaction-controlled dissolution-precipitation creep is the main mechanisms to generate recrystallized neoblasts in shear bands and strain shadows with a reasonable asymmetric monoclinic crystallographic fabric (Bons and Den Brok, 2000; Ribeiro et al., 2023). Since muscovite crystallization temperature relies on the Na–K content (Blencoe et al., 1994), muscovite recrystallization via dissolution-precipitation creep may occur under medium-temperature conditions, consistent with the deformation conditions of most mid-crustal shear zones (Ceccato et al., 2022).

Based on the microstructural observations and chemical data, we propose that these shear bands evolve from micro-cracks at high-angle to the (001) cleavage plane, accumulating strain and allowing metamorphic fluids to infiltrate the microstructure. The combination of high strain and fluid circulation in narrow microstructures induces mica recrystallization through dynamic recrystallization which involves coeval crystal-plastic deformation and dissolution-precipitation creep as highlighted by the high-spatial resolution EBSD and ToF-SIMS ion mapping, consistent with findings from Ribeiro et al. (2023). Thus, high-angle micro-cracks evolve to shear bands that accommodate grain size reduction and deformation which will likely evolve to micro shear zones displacing individual sub-mica fish at higher finite strain (see Fig. 5B).

6.3. Deformation impact on intragrain Rb–Sr single dates

Ar in deformed mineral grains such as feldspar and micas is known to heterogeneously diffuse to "microstructural pockets" leading to significantly distinct ages when analysed via in situ UV-laser ^{40}Ar/^{39}Ar (Mulch et al., 2002; Mulch and Cosca, 2004; Nteme et al., 2023; Reddy et al., 1996, 1999, 2001; Reddy and Potts, 1999). It has only recently been possible to acquire microstructurally controlled Rb–Sr isotopic measurements on a suitable scale via LA-TQ-ICP-MS, so the relationship between mica deformation and Rb–Sr single dates is unknown. We selected one coarse-grained muscovite fish from sample PS40A displaying a wide variation in strain from the core to the edge for gridding multiple Rb–Sr single spots to observe if any relationship between strain and Rb–Sr isotopes could be determined.

As explored previously, muscovite fish displays a mostly low strain
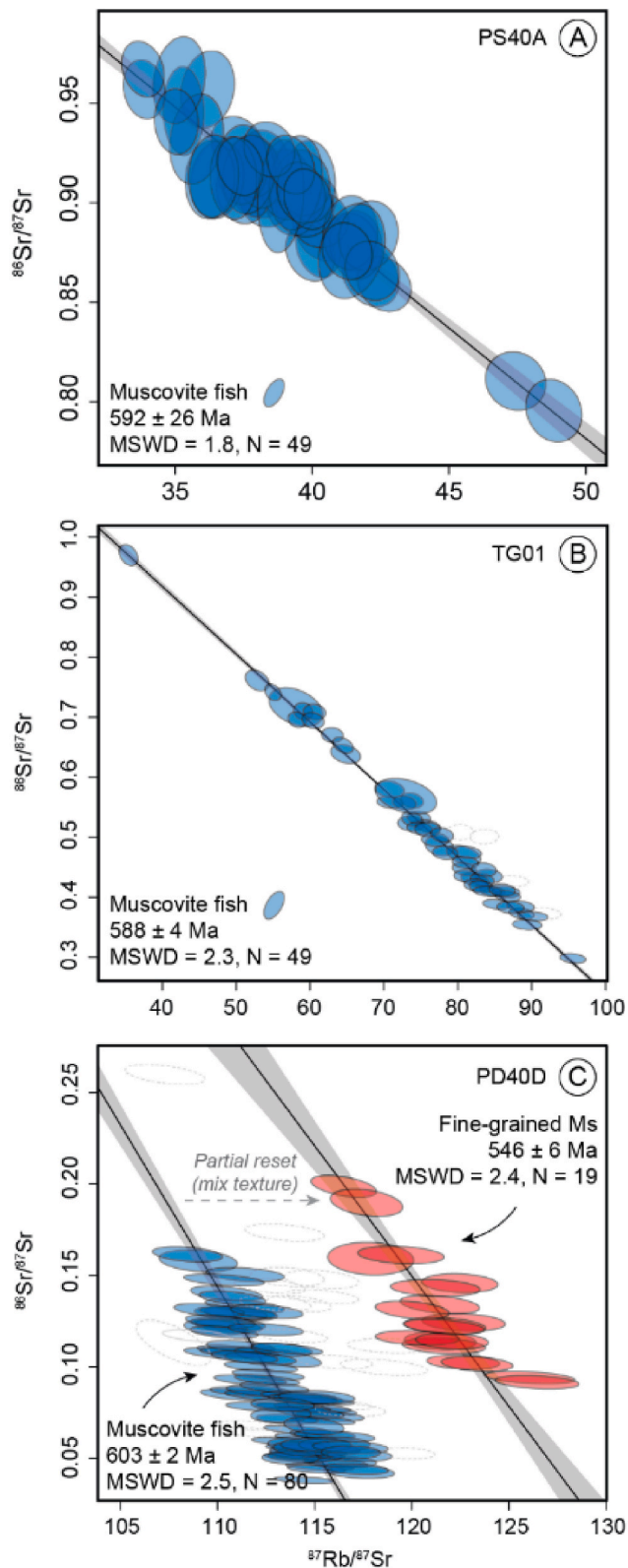
Fig. 10. Inverse Rb–Sr isochrons of muscovite fish grains from samples PS40A (A), TG01 (B), and of muscovite fish and fine-grained muscovite grains from PS40D (C) from the Taxaquara shear zone. Ellipse uncertainties and errors are presented at 2 standard error from the mean. Blue and red ellipses represent muscovite fish and low strain fine-grained muscovite, respectively. (For interpretation of the references to colour in this figure legend, the reader is referred to the Web version of this article.)

inner core as indicated by low GROD values, with strain increasing towards the grain edge (Fig. 12A). The Rb–Sr single spot contour age map indicates a good relationship between single dates and strain, with older dates preserved in the inner core (lower strain) and younger ages towards the grain edge (higher strain) (Fig. 12B and C). Yet, the differences between dates are not sufficient to resolve Rb–Sr single dates within the uncertainty of measurement for single muscovite fish in our case study despite the high apparent precision for in situ Rb–Sr single dates (up to 2.0 %). A similar relationship between muscovite fish internal strain and Rb–Sr single dates has been noted in Ribeiro et al. (2023), demonstrating that Rb–Sr single dates from the fish edges tend to rotate the Rb–Sr isochron towards younger ages disturbing the initial $^{87}Sr/^{86}Sr$ ratio. The modification to the initial $^{87}Sr/^{86}Sr$ ratio suggests that muscovite fish deformation occurs in an open-system where fluids are able to mobilise certain elements, as also inferred from secondary fluid inclusion tracks in syn-deformation recrystallized quartz (Ribeiro et al., 2023). However, the Rb–Sr single dates from coarse-grained muscovite fish presented here do not indicate any significant modification to the initial $^{87}Sr/^{86}Sr$ ratio, implying less influence from fluids during crystal-plastic deformation compared to fine-grained recrystallized muscovite in specific microstructures (e.g., shear bands and pressure shadows).

To further explore the relationship between internal strain and Rb–Sr single dates, additional high spatial resolution analysis such as transmission electron microscopy (TEM) or atom probe tomography (APT; Cappelli et al., 2022; Reddy et al., 2020) could help in accessing isotopic behaviour across dislocation boundaries. Although APT is a relatively new technique to study micas and reveal sub-nanometric chemical structures, it is challenging due to the complex interaction between the mica structure and the laser pulse upon a high electric field (Cappelli et al., 2022).

6.4. Rb–Sr isotopic behaviour in mica fish

Muscovite fish Rb–Sr dates from the medium-temperature Taxaquara shear zone (TSZ) are inconsistent with the timing of mylonitization previously constrained at c. 560–535 Ma based on apatite U–Pb and muscovite fish $^{40}Ar/^{39}Ar$ dates (Ribeiro et al., 2020b). Instead, muscovite fish Rb–Sr yields dates that constrain the crystallization of the protolith (Fig. 13A). Although the recent literature suggests that deformation is supposed to be the predominant factor in controlling the Rb–Sr geochronometer within relict muscovite below ~500 °C (Eberlei et al., 2015), this isotopic system within crystal-plastically deformed coarse-grained muscovite fish can remain unaffected by medium-grade mylonitization at P–T conditions of 480–530 °C and 2.2–5.0 kbar (Ribeiro et al., 2019, 2020a). Instead, recrystallized fine-grained muscovite in narrow shear bands and strain shadows are the only muscovite textures that yielded Rb–Sr dates consistent with the timing of mylonitization (Fig. 13A), suggesting that thermally activated volume-diffusion may be an inefficient way to isotopically reset the Rb–Sr isotopes in muscovite fish, at the temperatures these rocks were deformed at.

The lack of experimental data regarding Sr diffusion parameters in muscovite such as activation energy (E_a) and frequency factor (D_0) makes it difficult to estimate the Rb–Sr closure temperature using the Arrhenius equation (following Dodson, 1973). A range of closure temperatures between 450 and 600 °C have been proposed for muscovite Rb–Sr based on comparative geochronology with U–Pb dates from monazite, zircon and apatite, and K–Ar and $^{40}Ar/^{39}Ar$ dates from hornblende and micas (Eberlei et al., 2015; Freeman et al., 1997; Glodny et al., 1998, 2008; Kirkland et al., 2023; Ribeiro et al., 2022b; Von Blanckenburg et al., 1989). In cases where mylonitization temperature was theoretically high enough to stimulate Sr isotopic resetting through thermally activated volume diffusion, the isotopic system remained intact (e.g., Glodny et al., 2008; Ribeiro et al., 2023). Kühn et al. (2000) also demonstrated that Rb–Sr isotopes in phlogopite from Norwegian
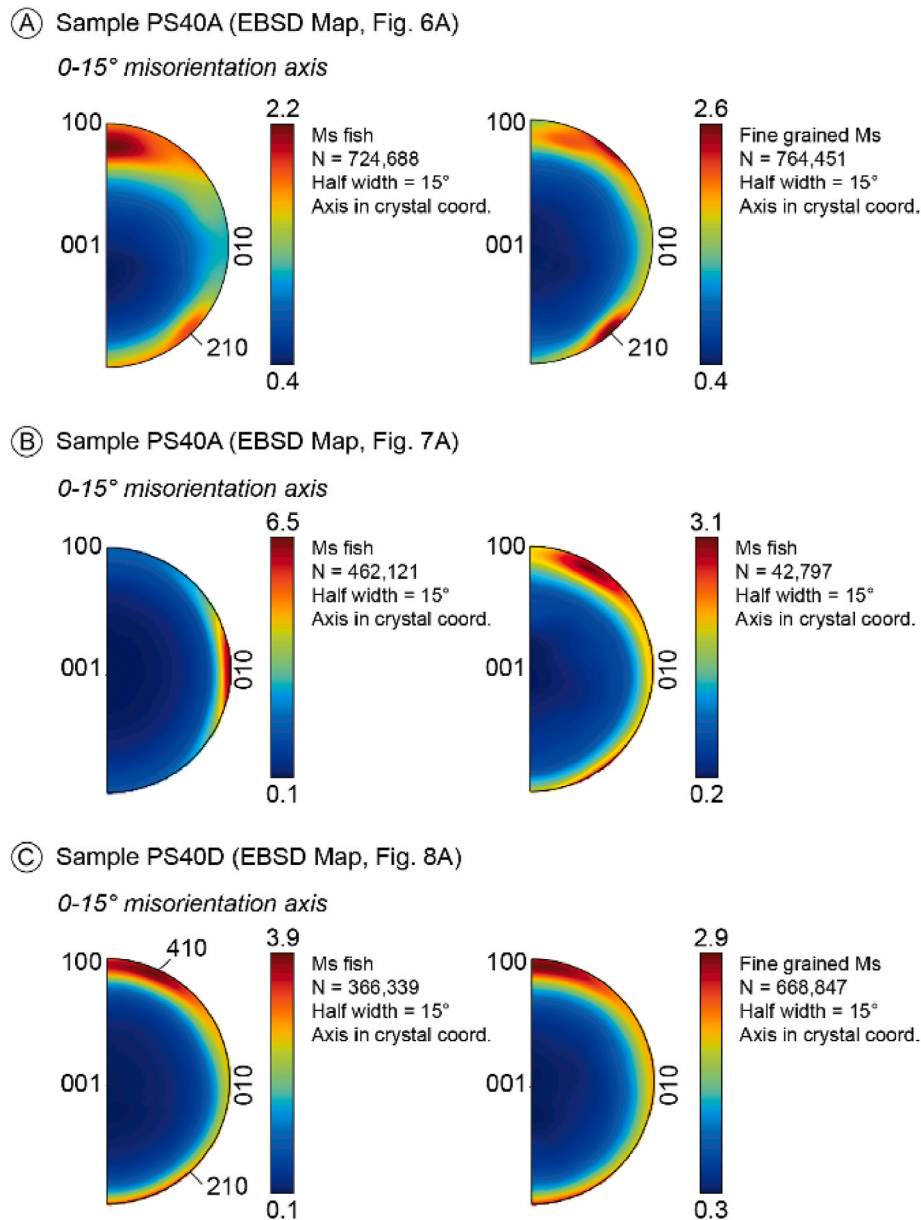
Fig. 11. Low-angle misorientation axis diagrams (crystal coordinates) of muscovite fish and fine-grained muscovite (tails) from the medium-temperature mylonites PS40A (A, B) and PS40D (C).

eclogites were only disturbed at temperature conditions of ~650 °C, higher than that typically expected (300–400 °C), which was attributed to fluid absent conditions that prevented element transport and re-homogenization. This literature and recent field examples suggest that temperature alone is frequently insufficient to reset the Sr isotopic memory of micas during ductile deformation via thermally activated volume diffusion (Glodny et al., 2008; Kirkland et al., 2023; Ribeiro et al., 2023).

Here, we infer the muscovite closure temperature for Rb–Sr isotopes using estimates of Sr diffusion parameters from Jenkin (1997) to empirically compare muscovite fish Rb–Sr and $^{40}Ar/^{39}Ar$ in light of thermochronology (i.e., isotopic-exchange mostly controlled by thermally activated volume diffusion). As empirically suggested in the literature, the inferred muscovite Sr closure temperature is systematically higher than muscovite Ar closure temperature using identical cooling rates and diffusion geometry (Fig. 13B). Since muscovite fish tend to be coarse-grained in most mylonites (up to ~1000 μm and median of ~800 μm in the medium-temperature mylonites from the TSZ),

this simplistic closure temperature model implies a minimum deformation temperature of ~600 °C to stimulate isotopic resetting via thermally-activated volume diffusion. From this, we conclude that the Rb–Sr isotopic system in coarse-grained muscovite fish is reset under or above amphibolite facies conditions (600–700 °C), bracketed at higher temperatures by the melt-in reactions due to muscovite breakdown. In contrast, the Ar isotopic system in muscovite fish matches the mylonitization conditions of many crustal shear zones (450–500 °C; Ceccato et al., 2022), suggesting it records the timing of deformation in many cases (e.g., Dunlap et al., 1991; Mulch and Cosca, 2004; Zhu et al., 2005, many others). However, the Ar isotopic system is extremely sensitive to secondary processes (e.g., metamorphism and fluid-rock interaction) and deformation-enhanced diffusion generally producing complex Ar spectra, radiogenic Ar loss and cryptic Ar excess (Kramar et al., 2003; Larson et al., 2023; Mulch et al., 2002; Nteme et al., 2023). Thus there are problems with both approaches, since Rb–Sr isotopic behaviour seems to be less affected by intragrain crystal-plastic deformation and less sensitive to isotopic resetting, whereas $^{40}Ar/^{39}Ar$ isotopic behaviour
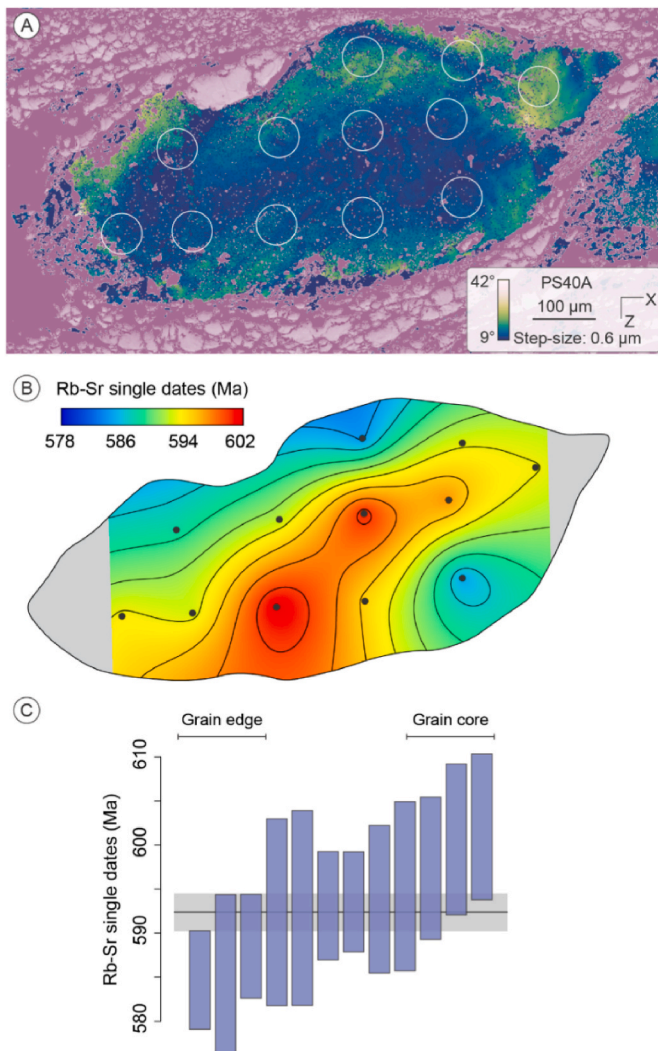
Fig. 12. A) Grain reference orientation deviation angle (GROD) maps of muscovite fish from sample PS40A; B) Contour-map of Rb–Sr single dates; C) Weighted Rb–Sr single dates from a single muscovite fish. Single dates were calculating using the initial $^{87}Sr/^{86}Sr$ ratio (0.748 ± 0.016) defined by the normal isochron. Rb–Sr single dates were contoured using Past4 software (Hames and Cheney, 1997) with a Kriging model using a 500 × 500 matrix size. Error-bars are presented at 2 standard error from the mean.

is typically reset through thermally-activated volume diffusion but is also highly sensitive to deformation-enhanced diffusion, likely leading to spurious data. This apparent impasse might be solved when targeting specific muscovite microstructures linked to deformation and recrystallization processes that promote grain size reduction in muscovite fish (Ribeiro et al., 2023).

As demonstrated here, muscovite fish is typically surrounded by fine-grained muscovite, mostly located in strain shadows (Fig. 5A, D; 6A, B), along muscovite fish-feldspar interfaces (Fig. 5B–D) and (rarely) across coarse-grained muscovite fish (Fig. 6C and D). Detailed EBSD mapping characterized these grains as low strain, displaying an asymmetric <001> single-girdle with dextral kinematics (Fig.. 7B and 9B), suggestive of recrystallization coeval with mylonitization. This recrystallization process led by crystal-plastic deformation and dissolution-precipitation creep is key for Rb–Sr isotopes, developing neoblasts with smaller effective diffusion length, which facilitate it to record the timing of recrystallization during mylonitization below the estimate closure temperature for coarse-grained mica fish, hence establishing a direct time-strain link in complexly deformed rocks (this study; Ribeiro
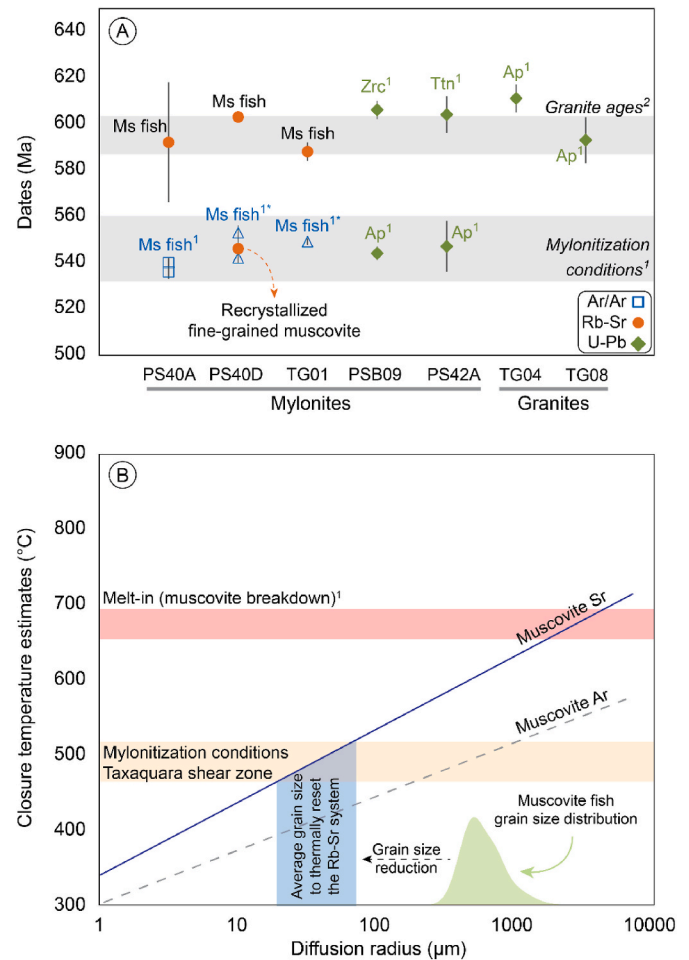
Fig. 13. A) Geochronology summary of the Taxaquara shear zone, SE Brazil. Muscovite fish $^{40}Ar/^{39}Ar$ dates, and zircon, titanite and apatite U–Pb dates are from Ribeiro et al. (2020b)[1]. Highlighted $^{40}Ar/^{39}Ar$ total fusion dates (*) from samples PS40D and TG01 were interpreted to reflect excess Ar. The timing of regional granitic magmatism follows previous published zircon and monazite U–Pb isotopic data (Janasi et al., 2001; Leite et al., 2007)[2]; B) Closure temperature modelling in muscovite using the estimate Sr parameters from Jenkin (1997) and Ar parameters from (Harrison et al., 2009). Closure temperature estimates were modelled using the classical equation from Dodson (1973). For simplistic reasons, we used an initial temperature of 400 °C for Sr and 300 °C for Ar, a planar diffusion geometry and a 10 °C/Ma cooling rate. [1]Red rectangle indicates the melt-in temperature (muscovite breakdown) from granitic mylonites from the Taxaquara shear zone (Ribeiro et al., 2019, 2020a). Kernel density estimates were constructed using the long axis of muscovite fish from the mylonitic samples from the Taxaquara shear zone. Fish grains were digitized in Adobe Illustrator™ (based on TIMA maps) and shape parameters were quantified using the SPO freeware (Launeau and Robin, 2003). (For interpretation of the references to colour in this figure legend, the reader is referred to the Web version of this article.)

et al., 2023). Thus, the timing of mylonitization may be determined by targeting muscovite microstructures associated with recrystallization mechanisms during in situ Rb–Sr analysis using a LA-TQ-ICP-MS system, which commonly yield Rb–Sr isochron and single dates associated with deformation with less influence of secondary processes such as those observed in the $^{40}Ar/^{39}Ar$ system (see Larson et al., 2023 for a systematic comparison between Rb–Sr and $^{40}Ar/^{39}Ar$ in deformed Himalayan rocks).

7. Conclusion

We provide a review on the evolution of mica fish and the effects of

deformation in the chemical-isotopic systems, also providing advances based on high-spatial resolution crystallographic (via EBSD) and chemical mapping (via ToF-SIMS), and in situ Rb–Sr isotopic analysis. The literature review combined with our new data highlight the importance of intracrystalline deformation during fish shape development, likely due to strain gradient from the mostly rigid muscovite core to the edges commonly affected by synthetic simple shear. The stored internal strain in muscovite also assist in the segregation of new and smaller muscovite fish taking advantage of high-angle micro-cracks that evolve to shear bands, accommodating grain size reduction, deformation and recrystallization, which evolve to micro shear zones displacing individual sub-mica fish during progressive mylonitization. Despite high degrees of intragrain crystal-plastic strain, mica fish accommodate deformation solely through low-angle basal slip given its strong anisotropy and the lack of multiple slip systems, which prevent it from developing microstructures such as subgrains. The complex intracrystalline disarrangement in mica fish is known to disturb the $^{40}Ar/^{39}Ar$ isotopic system (e.g., cryptic ^{40}Ar excess and ^{40}Ar loss), but our results suggest that the Rb–Sr system is less disrupted by intracrystalline deformation making it more suitable for dating complex deformed grains. Yet, the combination of slow Sr diffusivity and commonly coarse muscovite fish grain size push the Sr closure temperature towards ~600 °C or higher, thus muscovite fish may primarily date the protolith rather than the timing of deformation. However, given its ability to recrystallize through dynamic precipitation, mica is key to track time-strain evolution of complexly deformed rocks with syn-kinematically recrystallized micas along mica fish edges, strain shadows and shear bands commonly recording the timing of deformation.

Author statement

Bruno V. Ribeiro: Conceptualization, Investigation, Formal analysis, Data collection, Writing original draft. Christopher Kirkland: Conceptualization, Resources, Validation, Review and editing. Melanie Finch: Conceptualization, Validation, Review and editing. Frederico Faleiros: Conceptualization, Validation, Review and editing. Steven Reddy: Data collection, Validation, Review and editing. William Rickard: Data collection, Validation, Review and editing. Michael I.H. Hartnady: Validation, Review and editing.

Declaration of competing interest

The authors declare that they have no known competing financial interests or personal relationships that could have appeared to influence the work reported in this paper.

Data availability

The dataset is available in the online supplementary materials.

Acknowledgements

Appendix A. Supplementary data

Supplementary data to this article can be found online at https://doi.org/10.1016/j.jsg.2023.104947.

References

Airaghi, L., Warren, C.J., de Sigoyer, J., Lanari, P., Magnin, V., 2018. Influence of dissolution/reprecipitation reactions on metamorphic greenschist to amphibolite facies mica 40Ar/39Ar ages in the Longmen Shan (eastern Tibet). J. Metamorph. Geol. 36, 933–958. https://doi.org/10.1111/jmg.12420.

Alsop, G.I., Holdsworth, R.E., 2004. Shear zones — an introduction and overview. Geol. Soc. London, Special Publ. 224, 1. https://doi.org/10.1144/GSL.SP.2004.224.01.01. LP – 9.

Azor, A., Simancas, J.F., Exposito, I., Lodeiro, F.G., Martinez Poyatos, D.J., 1997. Deformation of garnets in a low-grade shear zone. J. Struct. Geol. 19, 1137–1148. https://doi.org/10.1016/S0191-8141(97)00040-0.

Bell, I.A., Wilson, C.J.L., 1981. Deformation of biotite and muscovite: TEM microstructure and deformation model. Tectonophysics 78, 201–228. https://doi.org/10.1016/0040-1951(81)90014-7.

Bell, I.A., Wilson, C.J.L., McLaren, A.C., Etheridge, M.A., 1986. Kinks in mica: role of dislocations and (001) cleavage. Tectonophysics 127, 49–65. https://doi.org/10.1016/0040-1951(86)90078-8.

Bestmann, M., Prior, D.J., Veltkamp, K.T.A., 2004. Development of single-crystal σ-shaped quartz porphyroclasts by dissolution–precipitation creep in a calcite marble shear zone. J. Struct. Geol. 26, 869–883. https://doi.org/10.1016/j.jsg.2003.10.003.

Blencoe, J.G., Guidotti, C.V., Sassi, F.P., 1994. The paragonite-muscovite solvus: II. Numerical geothermometers for natural, quasibinary paragonite-muscovite pairs. Geochem. Cosmochim. Acta 58, 2277–2288. https://doi.org/10.1016/0016-7037(94)90010-8.

Bons, P.D., Den Brok, B., 2000. Crystallographic preferred orientation development by dissolution-precipitation creep. J. Struct. Geol. 22, 1713–1722. https://doi.org/10.1016/S0191-8141(00)00075-4.

Cabrita, D.I.G., Faleiros, F.M., Cawood, P.A., Campanha, G.A.C., Yogi, M.T.A.G., Wainwright, A.N., Raveggi, M., Almeida, V.V., 2021. Petrochronological constraints and tectonic implications of tonian metamorphism in the Embu complex, Ribeira belt, Brazil. Precambrian Res. 363, 106315 https://doi.org/10.1016/j.precamres.2021.106315.

Cabrita, D.I.G., Faleiros, F.M., Ribeiro, B.v., Menegon, L., Cawood, P.A., Campanha, G.A. C., 2022. Deformation, Thermochronology and Tectonic Significance of the Crustal-Scale Cubatão Shear Zone, Ribeira Belt, Brazil. Tectonophysics 229278. https://doi.org/10.1016/j.tecto.2022.229278.

Campanha, G.A.C., Brito Neves, B.B., 2004. Frontal and oblique tectonics in the Brazilian Shield. Episodes 27, 255–259. https://doi.org/10.1016/S1342-937X(05)70391-9.

Campanha, G.A.C., Sadowski, G.R., 1999. Tectonics of the southern portion of the Ribeira belt (Apiaí domain). Precambrian Res. 98, 31–51. https://doi.org/10.1016/S0301-9268(99)00027-3.

Campanha, G.A.C., Faleiros, F.M., Cabrita, D.I.G., Ribeiro, B.V., Cawood, P.A., 2023. The southern Ribeira Belt in Western Gondwana: a record of a long-lived continental margin and terrane collage. J. South Am. Earth Sci. 127, 104404 https://doi.org/10.1016/j.jsames.2023.104404.

Campos Neto, M.C., 2000. Orogenic system from southwestern Gondwana: an approach to brasilian-pan afrian cycle and orogenic collage in southeastern Brazil. In: Tectonic Evolution of South America, pp. 335–365.

Cappelli, C., Pérez-Huerta, A., Alam, S.B., Prozorov, T., 2022. Atom probe tomography analysis of mica. Microsc. Microanal. 28, 1207–1220. https://doi.org/10.1017/S1431927621012940.

Carvalho, B.B., Sawyer, E.W., Janasi, V.A., 2016. Crustal reworking in a shear zone: transformation of metagranite to migmatite. J. Metamorph. Geol. 34, 237–264. https://doi.org/10.1111/jmg.12180.

Carvalho, B.B., Janasi, V.A., Sawyer, E.W., 2017. Evidence for Paleoproterozoic anatexis and crustal reworking of Archean crust in the São Francisco Craton, Brazil: a dating and isotopic study of the Kinawa migmatite. Precambrian Res. 291, 98–118. https://doi.org/10.1016/j.precamres.2017.01.019.

Caxito, F.A., Hartmann, L.A., Heilbron, M., Pedrosa-Soares, A.C., Bruno, H., Basei, M.A. S., Chemale, F., 2022. Multi-proxy evidence for subduction of the neoproterozoic adamastor ocean and Wilson cycle tectonics in the south atlantic brasiliano orogenic system of western Gondwana. Precambrian Res. 376, 106678 https://doi.org/10.1016/j.precamres.2022.106678.

Ceccato, A., Goncalves, P., Menegon, L., 2022. On the petrology and microstructures of small-scale ductile shear zones in granitoid rocks: an overview. J. Struct. Geol. 161, 104667 https://doi.org/10.1016/j.jsg.2022.104667.

Challandes, N., Marquer, D., Villa, I.M., 2003. Dating the evolution of C-S microstructures: a combined 40Ar/39Ar step-heating and UV laserprobe analysis of the Alpine Roffna shear zone. Chem. Geol. 197, 3–19. https://doi.org/10.1016/S0009-2541(02)00354-6.

Challandes, N., Marquer, D., Villa, I.M., 2008. P-T-t modelling, fluid circulation, and 39Ar-40Ar and Rb-Sr mica ages in the Aar Massif shear zones (Swiss Alps). Swiss J. Geosci. 101, 269–288. https://doi.org/10.1007/s00015-008-1260-6.

Chen, C.-T., Chan, Y.-C., Lo, C.-H., Lu, C.-Y., 2016. Growth of mica porphyroblasts under low-grade metamorphism – a Taiwanese case using in-situ 40Ar/39Ar laser microprobe dating. J. Struct. Geol. 92, 1–11. https://doi.org/10.1016/j.jsg.2016.09.005.

Cheng, P., Koyanagi, G.K., Bohme, D.K., 2008. On the chemical resolution of the 87Rb+ (s0)/87Sr+ (s1) isobaric interference: a kinetic search for an optimum reagent. Anal. Chim. Acta 627, 148–153. https://doi.org/10.1016/j.aca.2008.03.057.

Cioffi, C.R., Campos Neto, M. da C., Möller, A., Rocha, B.C., 2019. Titanite petrochronology of the southern Brasília Orogen basement: effects of retrograde net-transfer reactions on titanite trace element compositions. Lithos 344 (345), 393–408. https://doi.org/10.1016/j.lithos.2019.06.035.

Conte, T., Cavalcante, C., Lagoeiro, L.E., Fossen, H., Silveira, C.S., 2020. Quartz textural analysis from an anastomosing shear zone system: implications for the tectonic evolution of the Ribeira belt, Brazil. J. South Am. Earth Sci. 103, 102750 https://doi.org/10.1016/j.jsames.2020.102750.

Cosca, M., Stunitz, H., Bourgeix, A.-L., Lee, J.P., 2011. 40Ar* loss in experimentally deformed muscovite and biotite with implications for 40Ar/39Ar geochronology of naturally deformed rocks. Geochem. Cosmochim. Acta 75, 7759–7778. https://doi.org/10.1016/j.gca.2011.10.012.

Cross, A.J., Prior, D.J., Stipp, M., Kidder, S., 2017. The recrystallized grain size piezometer for quartz: an EBSD-based calibration. Geophys. Res. Lett. 44, 6667–6674. https://doi.org/10.1002/2017GL073836.

Dell'angelo, L.N., Tullis, J., 1989. Fabric development in experimentally sheared quartzites. Tectonophysics 169, 1–21. https://doi.org/10.1016/0040-1951(89)90180-7.

Dickin, A.P., 2018. Radiogenic Isotope Geology. Cambridge University Press. https://doi.org/10.1017/9781316163009.

Dodson, M.H., 1973. Closure temperature in cooling geochronological and petrological systems. Contrib. Mineral. Petrol. 40, 259–274.

Dunlap, W.J., 1997. Neocrystallization or cooling?40Ar/39Ar ages of white micas from low-grade mylonites. Chem. Geol. 143, 181–203. https://doi.org/10.1016/S0009-2541(97)00113-7.

Dunlap, W.J., Teyssier, C., McDougall, I., Baldwin, S., 1991. Ages of deformation from K/Ar and 40Ar/39Ar dating of white micas. Geology 19, 1213. https://doi.org/10.1130/0091-7613(1991)019<1213:AODFKA>2.3.CO;2.

Eberlei, T., Habler, G., Wegner, W., Schuster, R., Körner, W., Thöni, M., Abart, R., 2015. Rb/Sr isotopic and compositional retentivity of muscovite during deformation. Lithos 227, 161–178. https://doi.org/10.1016/j.lithos.2015.04.007.

Egydio-Silva, M., Vauchez, A., Bascou, J., Hippertt, J., 2002. High-temperature deformation in the Neoproterozoic transpressional Ribeira belt, southeast Brazil. Tectonophysics 352, 203–224. https://doi.org/10.1016/S0040-1951(02)00197-X.

Egydio-Silva, M., Vauchez, A., Raposo, M.I.B., Bascou, J., Uhlein, A., 2005. Deformation regime variations in an arcuate transpressional orogen (Ribeira belt, SE Brazil) imaged by anisotropy of magnetic susceptibility in granulites. J. Struct. Geol. 27, 1750–1764. https://doi.org/10.1016/j.jsg.2005.06.001.

Egydio-Silva, M., Vauchez, A., Fossen, H., Gonçalves Cavalcante, G.C., Xavier, B.C., 2018. Connecting the Araçuaí and Ribeira belts (SE – Brazil): progressive transition from contractional to transpressive strain regime during the Brasiliano orogeny. J. South Am. Earth Sci. 86, 127–139. https://doi.org/10.1016/j.jsames.2018.06.005.

Erickson, T.M., Pearce, M.A., Taylor, R.J.M., Timms, N.E., Clark, C., Reddy, S.M., Buick, I.S., 2015. Deformed monazite yields high-temperature tectonic ages. Geology 43, 383–386. https://doi.org/10.1130/G36533.1.

Etheridge, M.A., Hobbs, B.E., 1974. Chemical and deformational controls on recrystallization of mica. Contrib. Mineral. Petrol. 43, 111–124. https://doi.org/10.1007/BF00572714.

Etheridge, M.A., Hobbs, B.E., Paterson, M.S., 1973. Experiental deformation of single crystals of biotite. Contrib. Mineral. Petrol. 38, 21–36. https://doi.org/10.1007/BF00371724.

Faleiros, F.M., Campanha, G.A.C., Martins, L., Vlach, S.R.F., Vasconcelos, P.M., 2011. Ediacaran high-pressure collision metamorphism and tectonics of the southern Ribeira Belt (SE Brazil): evidence for terrane accretion and dispersion during Gondwana assembly. Precambrian Res. 189, 263–291.

Faleiros, F.M., Ribeiro, B.V., Campanha, G.A.C., Cawood, P.A., Cabrita, D.I.G., Yogi, M.T. A.G., Milani, L.A., Lemos-Santos, D.V., Almeida, V.V., Rodrigues, S.W.O., Malta, I.S., Forero-Ortega, A.J., 2022. Strain Partitioning along Terrane Bounding and Intraterrane Shear Zones: Constraints from a Long-Lived Transpressional System in West Gondwana (Ribeira Belt, Brazil). https://doi.org/10.2113/2022/2103213. Lithosphere 2022.

Finch, M.A., Weinberg, R.F., Hasalová, P., Becchio, R., Fuentes, M.G., Kennedy, A., 2017. Tectono-metamorphic evolution of a convergent back-arc: the famatinian orogen, sierra de Quilmes, sierras pampeanas, NW Argentina. GSA Bullet. https://doi.org/10.1130/B31620.1.

Forero-Ortega, A.J., Campanha, G.A.C., Faleiros, F.M., Yogi, M.T.A.G., 2020. Pure shear-dominated transpression and vertical extrusion in a strike-slip fault splay from the Itapirapuã Shear Zone, Ribeira Belt, Brazil. Tectonophysics 786, 228455. https://doi.org/10.1016/j.tecto.2020.228455.

Fossen, H., Cavalcante, G.C.G., 2017. Shear zones – a review. Earth Sci. Rev. 171, 434–455. https://doi.org/10.1016/j.earscirev.2017.05.002.

Fougerouse, D., Cavosie, A.J., Erickson, T., Reddy, S.M., Cox, M.A., Saxey, D.W., Rickard, W.D.A., Wingate, M.T.D., 2021a. A new method for dating impact events – thermal dependency on nanoscale Pb mobility in monazite shock twins. Geochem. Cosmochim. Acta 314, 381–396. https://doi.org/10.1016/j.gca.2021.08.025.

Fougerouse, D., Reddy, S.M., Seydoux-Guillaume, A.-M., Kirkland, C.L., Erickson, T.M., Saxey, D.W., Rickard, W.D.A., Jacob, D., Leroux, H., Clark, C., 2021b. Mechanical twinning of monazite expels radiogenic lead. Geology 49, 417–421. https://doi.org/10.1130/G48400.1.

Freeman, S.R., Inger, S., Butler, R.W.H., Cliff, R.A., 1997. Dating deformation using Rb-Sr in white mica: greenschist facies deformation ages from the Entrelor shear zone, Italian Alps. Tectonics 16, 57–76. https://doi.org/10.1029/96TC02477.

García-Ruiz, S., Moldovan, M., García Alonso, J.I., 2008. Measurement of strontium isotope ratios by MC-ICP-MS after on-line Rb–Sr ion chromatography separation. J. Anal. At. Spectrom. 23, 84–93. https://doi.org/10.1039/B708936H.

Giraldo, S.J., Trouw, R.A.J., Duffles, P., Vinagre, R., Mejia, M.I., Marimon, R.S., 2019. Structural analysis combined with new geothermobarometric and geochronological results of the Além Paraíba shear zone, between Três Rios and Bananal, Ribeira Orogen, SE Brazil. J. South Am. Earth Sci. 90, 118–136. https://doi.org/10.1016/j.jsames.2018.11.018.

Glodny, J., Grauert, B., Fiala, J., Vejnar, Z., Krohe, A., 1998. Metapegmatites in the western Bohemian massif: ages of crystallisation and metamorphic overprint, as constrained by U-Pb zircon, monazite, garnet, columbite and Rb-Sr muscovite data. Geol. Rundsch. 87, 124–134. https://doi.org/10.1007/s005310050194.

Glodny, J., Kühn, A., Austrheim, H., 2008. Diffusion versus recrystallization processes in Rb–Sr geochronology: isotopic relics in eclogite facies rocks, Western Gneiss Region, Norway. Geochem. Cosmochim. Acta 72, 506–525. https://doi.org/10.1016/j.gca.2007.10.021.

Glorie, S., Otasevic, A., Gillespie, J., Jepson, G., Danišík, M., Zhimulev, F.I., Gurevich, D., Zhang, Z., Song, D., Xiao, W., 2019. Thermo-tectonic history of the junggar alatau within the central asian orogenic belt (SE Kazakhstan, NW China): insights from integrated apatite U/Pb, fission track and (U–Th)/He thermochronology. Geosci. Front. 10, 2153–2166. https://doi.org/10.1016/j.gsf.2019.05.005.

Gordon, S.M., Kirkland, C.L., Reddy, S.M., Blatchford, H.J., Whitney, D.L., Teyssier, C., Evans, N.J., McDonald, B.J., 2021. Deformation-enhanced recrystallization of titanite drives decoupling between U-Pb and trace elements. Earth Planet Sci. Lett. 560, 116810 https://doi.org/10.1016/j.epsl.2021.116810.

Goscombe, B., Gray, D., Armstrong, R., Foster, D.A., Vogl, J., 2005. Event geochronology of the pan-african kaoko belt, Namibia. Precambrian Res. 140 https://doi.org/10.1016/j.precamres.2005.07.003, 103.e1-103.e41.

Gray, D.R., Foster, D.A., Goscombe, B., Passchier, C.W., Trouw, R.A.J., 2006. 40Ar/39Ar thermochronology of the Pan-African Damara Orogen , Namibia , with implications for tectonothermal and geodynamic evolution. Precambrian Res. 150, 49–72. https://doi.org/10.1016/j.precamres.2006.07.003.

Gutiérrez-Alonso, G., Collins, A.S., Fernández-Suárez, J., Pastor-Galán, D., González-Clavijo, E., Jourdan, F., Weil, A.B., Johnston, S.T., 2015. Dating of lithospheric buckling: 40Ar/39Ar ages of syn-orocline strike-slip shear zones in northwestern Iberia. Tectonophysics 643, 44–54. https://doi.org/10.1016/j.tecto.2014.12.009.

Gyomlai, T., Agard, P., Jolivet, L., Larvet, T., Bonnet, G., Omrani, J., Larson, K., Caron, B., Noël, J., 2022. Cimmerian metamorphism and post Mid-Cimmerian exhumation in Central Iran: insights from in-situ Rb/Sr and U/Pb dating. J. Asian Earth Sci. 233, 105242 https://doi.org/10.1016/j.jseaes.2022.105242.

Hames, W.E., Cheney, J.T., 1997. On the loss of from muscovite during polymetamorphism. Geochem. Cosmochim. Acta 61, 3863–3872. https://doi.org/10.1016/S0016-7037(97)00207-X.

Harrison, T.M., Célérier, J., Aikman, A.B., Hermann, J., Heizler, M.T., 2009. Diffusion of40Ar in muscovite. Geochem. Cosmochim. Acta 73, 1039–1051. https://doi.org/10.1016/j.gca.2008.09.038.

Heilbron, M., de Morisson Valeriano, C., Peixoto, C., Tupinambá, M., Neubauer, F., Dussin, I., Corrales, F., Bruno, H., Lobato, M., Horta de Almeida, J.C., Guilherme do Eirado Silva, L., 2020. Neoproterozoic magmatic arc systems of the central Ribeira belt, SE-Brazil, in the context of the West-Gondwana pre-collisional history: a review. J. South Am. Earth Sci. 103, 102710 https://doi.org/10.1016/j.jsames.2020.102710.

Heisbacher, G.H., 1970. Deformation mechanics of mylonitic rocks and fractured granites in cobequid mountains, nova scotia, Canada. GSA Bullet. 81, 2009. –2020.

Hickman, M.H., Glassley, W.E., 1984. The role of metamorphic fluid transport in the Rb-Sr isotopic resetting of shear zones: evidence from Nordre Strømfjord, West Greenland. Contrib. Mineral. Petrol. 87, 265–281. https://doi.org/10.1007/BF00373060.

Hogmalm, K.J., Zack, T., Karlsson, A.K., Sjoqvist, A.S.L., Grabe-Schonberg, D., 2017. In-situ Rb-Sr and K-Ca dating by LA-ICP-MS/MS: an evaluation of N2O and SF6 as reaction gases. J Anal At Spectrom 32, 305–313.

Hueck, M., Wemmer, K., Basei, M.A.S., Philipp, R.P., Oriolo, S., Heidelbach, F., Oyhantçabal, P., Siegesmund, S., 2020. Dating recurrent shear zone activity and the transition from ductile to brittle deformation: white mica geochronology applied to the Neoproterozoic Dom Feliciano Belt in South Brazil. J. Struct. Geol. 141, 104199 https://doi.org/10.1016/j.jsg.2020.104199.

Hueck, M., Wemmer, K., Ksienzyk, A.K., Kuehn, R., Vogel, N., 2022. Potential, premises, and pitfalls of interpreting illite argon dates - a case study from the German Variscides. Earth Sci. Rev. 232, 104133 https://doi.org/10.1016/j.earscirev.2022.104133.

Inger, S., 1998. Timing of an extensional detachment during convergent orogeny: new Rb-Sr geochronological data from the Zanskar shear zone, northwestern Himalaya. Geology 26, 223. https://doi.org/10.1130/0091-7613(1998)026<0223:TOAEDD>2.3.CO;2.

Janasi, V.A., Leite, R.J., van Schmus, W.R., 2001. U-Pb chronostratigraphy of the granitic magmatism in the agudos grandes batholith (west of São Paulo, Brazil) - implications for the evolution of the Ribeira belt. J. South Am. Earth Sci. 14, 363–376. https://doi.org/10.1016/S0895-9811(01)00034-7.

Jenkin, G.R.T., 1997. Do cooling paths derived from mica Rb-Sr data reflect true cooling paths? Geology 25, 907. https://doi.org/10.1130/0091-7613(1997)025<0907:DCPDFM>2.3.CO;2.

Jenkin, G.R.T., Rogers, G., Fallick, A.E., Farrow, C.M., 1995. Rb-Sr closure temperatures in bi-mineralic rocks: a mode effect and test for different diffusion models. Chem. Geol. 122, 227–240. https://doi.org/10.1016/0009-2541(95)00013-C.

Ji, S., Martignole, J., 1994. Ductility of garnet as an indicator of extremely high temperature deformation. J. Struct. Geol. 16, 985–996. https://doi.org/10.1016/0191-8141(94)90080-9.

Kavanagh-Lepage, C., Gervais, F., Larson, K., Grazziani, R., Moukhsil, A., 2022. Deformation induced decoupling between U-Pb and trace elements in titanite revealed through petrochronology and study of localized deformation. Geosci. Front., 101496 https://doi.org/10.1016/j.gsf.2022.101496.

Kellett, D.A., Warren, C., Larson, K.P., Zwingmann, H., van Staal, C.R., Rogers, N., 2016. Influence of deformation and fluids on Ar retention in white mica: dating the dover fault, newfoundland appalachians. Lithos 254–255, 1–17. https://doi.org/10.1016/j.lithos.2016.03.003.

Kelley, S., 1995. Ar-Ar dating by laser microprobe. In: Microprobe Techniques in the Earth Sciences. Springer US, Boston, MA, pp. 327–358. https://doi.org/10.1007/978-1-4615-2053-5_8.

Kelley, S., 2002. K-Ar and Ar-Ar dating. Rev. Mineral. Geochem. 47, 785–818. https://doi.org/10.2138/rmg.2002.47.17.

Kirkland, C.L., Daly, J.S., Eide, E.A., Whitehouse, M.J., 2007. Tectonic evolution of the Arctic Norwegian Caledonides from a texturally- and structurally-constrained multi-isotopic (Ar-Ar, Rb-Sr, Sm-Nd, U-Pb) study. Am. J. Sci. 307, 459–526. https://doi.org/10.2475/02.2007.06.

Kirkland, C.L., Hollis, J., Danišík, M., Petersen, J., Evans, N.J., McDonald, B.J., 2017. Apatite and titanite from the Karrat Group, Greenland; implications for charting the thermal evolution of crust from the U-Pb geochronology of common Pb bearing phases. Precambrian Res. 300, 107–120. https://doi.org/10.1016/j.precamres.2017.07.033.

Kirkland, C.L., Olierook, H.K.H., Danišík, M., Liebmann, J., Hollis, J., Ribeiro, B.v., Rankenburg, K., 2023. Dating mylonitic overprinting of ancient rocks. Commun. Earth Environ. 4, 47. https://doi.org/10.1038/s43247-023-00709-5.

Kirschner, D.L., Cosca, M.A., Masson, H., Hunziker, J.C., 1996. Staircase 40Ar/39Ar spectra of fine-grained white mica: timing and duration of deformation and empirical constraints on argon diffusion. Geology 24, 747–750. https://doi.org/10.1130/0091-7613(1996)024<0747:SAASOF>2.3.CO;2.

Kligfield, R., Hunziker, J., Dallmeyer, R.D., Schamel, S., 1986. Dating of deformation phases using K-Ar and 40Ar/39Ar techniques: results from the Northern Apennines. J. Struct. Geol. 8, 781–798.

Kohn, M.J., 2018. Titanite petrochronology. Rev. Mineral. Geochem. 83, 419–441. https://doi.org/10.2138/rmg.2017.83.13.

Kramar, N., Cosca, M.A., Hunziker, J.C., 2001. Heterogeneous 40Ar* distributions in naturally deformed muscovite: in situ UV-laser ablation evidence for microstructurally controlled intragrain diffusion. Earth Planet Sci. Lett. 192, 377–388. https://doi.org/10.1016/S0012-821X(01)00456-3.

Kramar, N., Cosca, M.A., Buffatm, P.-A., Baumgartner, L.P., 2003. Stacking fault-enhanced argon diffusion in naturally deformed muscovite. Geochronology: Link. Isotopic Record with Petrol. text. 220, 249–260.

Kühn, A., Glodny, J., Iden, K., Austrheim, H., 2000. Retention of precambrian Rb/Sr phlogopite ages through caledonian eclogite facies metamorphism, bergen arc complex, W-Norway. Lithos 51, 305–330. https://doi.org/10.1016/S0024-4937(99)00067-5.

Larson, K.P., Button, M., Shrestha, S., Camacho, A., 2023. A comparison of 87Rb/87Sr and 40Ar/39Ar dates: evaluating the problem of excess 40Ar in Himalayan mica. Earth Planet Sci. Lett. 609, 118058 https://doi.org/10.1016/j.epsl.2023.118058.

Launeau, P., Robin, P.Y.F., 2003. SPO..

Leite, R.J., de Assis Janasi, V., Creaser, R.A., Heaman, L.M., 2007. The late- to postorogenic transition in the Apiaí domain, SE Brazil: constraints from the petrogenesis of the neoproterozoic agudos grandes granite batholith. J. South Am. Earth Sci. 23, 213–235. https://doi.org/10.1016/j.jsames.2006.09.003.

Li, Y., Vermeesch, P., 2021. Inverse isochron regression for Re-Os, K-Ca and other chronometers. Geochronol. Preprint. https://doi.org/10.5194/gchron-2021-7.

Liebmann, J., Kirkland, C.L., Kelsey, D.E., Korhonen, F.J., Rankenburg, K., 2022. Lithological fabric as a proxy for Rb–Sr isotopic complexity. Chem. Geol. 608, 121041 https://doi.org/10.1016/j.chemgeo.2022.121041.

Lister, G.S., Snoke, A.W., 1984. S-C mylonites. J. Struct. Geol. 6, 617–638. https://doi.org/10.1016/0191-8141(84)90001-4.

Mancktelow, N.S., 2002. Finite-element modelling of shear zone development in viscoelastic materials and its implications for localisation of partial melting. J. Struct. Geol. 24, 1045–1053. https://doi.org/10.1016/S0191-8141(01)00090-6.

Mares, V.M., Kronenberg, A.K., 1993. Experimental deformation of muscovite. J. Struct. Geol. 15, 1061–1075. https://doi.org/10.1016/0191-8141(93)90156-5.

Meike, A., 1989. In situ deformation of micas; a high-voltage electron-microscope study. Am. Mineral. 74, 780–796.

Meira, V.T., García-Casco, A., Juliani, C., Almeida, R.P., Schorscher, J.H.D., 2015. The role of intracontinental deformation in supercontinent assembly: insights from the Ribeira belt, southeastern Brazil (neoproterozoic West Gondwana). Terra. Nova 27, 206–217. https://doi.org/10.1111/ter.12149.

Meira, V.T., Garcia-Casco, A., Hyppolito, T., Juliani, C., Schorscher, J.H.D., 2019. Tectono-metamorphic evolution of the central Ribeira belt, Brazil: a case of late neoproterozoic intracontinental orogeny and flow of partially molten deep crust during the assembly of West Gondwana. Tectonics 38, 3182–3209. https://doi.org/10.1029/2018TC004959.

Moens, L.J., Vanhaecke, F.F., Bandura, D.R., Baranov, V.I., Tanner, S.D., 2001. Elimination of isobaric interferences in ICP-MS, using ion–molecule reaction chemistry: Rb/Sr age determination of magmatic rocks, a case study. J. Anal. At. Spectrom. 16, 991–994. https://doi.org/10.1039/B103707M.

Mora, C.A.S., Campanha, G.A., da, C., Wemmer, K., 2013. Microstructures and K-Ar illite fine-fraction ages of the cataclastic rocks associated to the camburu shear zone,

Ribeira belt, southeastern Brazil. Braz. J. Genet. 43, 607–622. https://doi.org/10.5327/z2317-48892013000400003.

Moser, A.C., Hacker, B.R., Gehrels, G.E., Seward, G.G.E., Kylander-Clark, A.R.C., Garber, J.M., 2022. Linking titanite U–Pb dates to coupled deformation and dissolution–reprecipitation. Contrib. Mineral. Petrol. 177, 42. https://doi.org/10.1007/s00410-022-01906-9.

Mukherjee, S., 2011. Mineral fish: their morphological classification, usefulness as shear sense indicators and genesis. Int. J. Earth Sci. 100, 1303–1314. https://doi.org/10.1007/s00531-010-0535-0.

Mulch, A., Cosca, M.A., 2004. Recrystallization or cooling ages: in situ UV-laser 40Ar/39Ar geochronology of muscovite in mylonitic rocks. J. Geol. Soc. London 161, 573–582. https://doi.org/10.1144/0016-764903-110.

Mulch, A., Cosca, M., Handy, M., 2002. In-situ UV-laser 40Ar/39Ar geochronology of a micaceous mylonite: an example of defect-enhanced argon loss. Contrib. Mineral. Petrol. 142, 738–752. https://doi.org/10.1007/s00410-001-0325-6.

Müller, W., Aerden, D., Halliday, A.N., 2000a. Isotopic dating of strain fringe increments: duration and rates of deformation in shear zones. Science 1979 (288), 2195–2198. https://doi.org/10.1126/science.288.5474.2195.

Müller, W., Mancktelow, N.S., Meier, M., 2000b. Rb–Sr microchrons of synkinematic mica in mylonites: an example from the DAV fault of the Eastern Alps. Earth Planet Sci. Lett. 180, 385–397. https://doi.org/10.1016/S0012-821X(00)00167-9.

Nebel, O., Scherer, E.E., Mezger, K., 2011. Evaluation of the 87Rb decay constant by age comparison against the U–Pb system. Earth Planet Sci. Lett. 301, 1–8. https://doi.org/10.1016/j.epsl.2010.11.004.

Nteme, J., Scaillet, S., Gardés, E., Duval, F., Nabelek, P., Mottolese, A., 2023. Defect-controlled 40Ar diffusion-domain structure of white micas from high-resolution 40Ar/39Ar crystal-mapping in slowly-cooled muscovite. Geochem. Cosmochim. Acta 342, 84–107. https://doi.org/10.1016/j.gca.2022.12.004.

Odlum, M.L., Levy, D.A., Stockli, D.F., Stockli, L.D., DesOrmeau, J.W., 2022. Deformation and metasomatism recorded by single-grain apatite petrochronology. Geology. https://doi.org/10.1130/G49809.1.

Olierook, H.K.H., Rankenburg, K., Ulrich, S., Kirkland, C.L., Evans, N.J., Brown, S., McInnes, B.I.A., Prent, A., Gillespie, J., McDonald, B., Darragh, M., 2020. Resolving multiple geological events using in situ Rb–Sr geochronology: implications for metallogenesis at Tropicana, Western Australia. Geochronology 2, 283–303. https://doi.org/10.5194/gchron-2-283-2020.

Oliver, D.H., Goodge, J.W., 1996. Leucoxene fish as a micro-kinematic indicator. J. Struct. Geol. 18, 1493–1497. https://doi.org/10.1016/S0191-8141(96)00067-3.

Oriolo, S., Oyhantçabal, P., Heidelbach, F., Wemmer, K., Siegesmund, S., 2015. Structural evolution of the Sarandí del Yí Shear Zone, Uruguay: kinematics, deformation conditions and tectonic significance. Int. J. Earth Sci. 104, 1759–1777. https://doi.org/10.1007/s00531-015-1166-2.

Oriolo, S., Oyhantçabal, P., Wemmer, K., Basei, M.A.S., Benowitz, J., Pfänder, J., Hannich, F., Siegesmund, S., 2016. Timing of deformation in the Sarandí del Yí Shear Zone, Uruguay: implications for the amalgamation of western Gondwana during the Neoproterozoic Brasiliano-Pan-African Orogeny. Tectonics 35, 754–771. https://doi.org/10.1002/2015TC004052.

Oriolo, S., Wemmer, K., Oyhantçabal, P., Fossen, H., Schulz, B., Siegesmund, S., 2018. Geochronology of shear zones – a review. Earth Sci. Rev. 185, 665–683. https://doi.org/10.1016/j.earscirev.2018.07.007.

Oriolo, S., Schulz, B., Hueck, M., Oyhantçabal, P., Heidelbach, F., Sosa, G., van den Kerkhof, A., Wemmer, K., Fossen, H., Druguet, E., Walter, J., Cavalcante, C., Siegesmund, S., 2022. The petrologic and petrochronologic record of progressive vs polyphase deformation: opening the analytical toolbox. Earth Sci. Rev., 104235 https://doi.org/10.1016/j.earscirev.2022.104235.

Papapavlou, K., Darling, J.R., Storey, C.D., Lightfoot, P.C., Moser, D.E., Lasalle, S., 2017. Dating shear zones with plastically deformed titanite: new insights into the orogenic evolution of the Sudbury impact structure (Ontario, Canada). Precambrian Res. 291, 220–235. https://doi.org/10.1016/j.precamres.2017.01.007.

Passchier, C.W., Simpson, C., 1986. Porphyroclast systems as kinematic indicators. J. Struct. Geol. 8, 831–843. https://doi.org/10.1016/0191-8141(86)90029-5.

Passchier, C.W., Trouw, R.A.J., 2005. Microtectonics, second ed. Springer, Boston, Mass.

Paton, C., Hellstrom, J., Paul, B., Woodhead, J., Hergt, J., 2011. Iolite: freeware for the visualisation and processing of mass spectrometric data. J Anal At Spectrom 26, 2508. https://doi.org/10.1039/c1ja10172b.

Pennacchioni, G., Di Toro, G., Mancktelow, N.S., 2001. Strain-insensitive preferred orientation of porphyroclasts in Mont Mary mylonites. J. Struct. Geol. 23, 1281–1298. https://doi.org/10.1016/S0191-8141(00)00189-9.

Platt, J.P., 2015. Rheology of two-phase systems: a microphysical and observational approach. J. Struct. Geol. 77, 213–227. https://doi.org/10.1016/j.jsg.2015.05.003.

Prior, D.J., Wheeler, J., 1999. Feldspar fabrics in a greenschist facies albite-rich mylonite from electron backscatter diffraction. Tectonophysics 303, 29–49. https://doi.org/10.1016/S0040-1951(98)00257-1.

Ramsay, J.G., 1980. Shear zone geometry: a review. J. Struct. Geol. 2, 83–99. https://doi.org/10.1016/0191-8141(80)90038-3.

Redaa, A., Farkaš, J., Gilbert, S., Collins, A.S., Wade, B., Löhr, S., Zack, T., Garbe-Schönberg, D., 2021. Assessment of elemental fractionation and matrix effects during in situ Rb–Sr dating of phlogopite by LA-ICP-MS/MS: implications for the accuracy and precision of mineral ages. J Anal At Spectrom 36, 322–344. https://doi.org/10.1039/D0JA00299B.

Reddy, S.M., Potts, G.J., 1999. Constraining absolute deformation ages: the relationship between deformation mechanisms and isotope systematics. J. Struct. Geol. 21, 1255–1265. https://doi.org/10.1016/S0191-8141(99)00032-2.

Reddy, S.M., Kelley, S.P., Wheeler, J., 1996. A 40Ar/39Ar laser probe study of micas from the Sesia Zone, Italian Alps: implications for metamorphic and deformation

histories. J. Metamorph. Geol. 14, 493–508. https://doi.org/10.1046/j.1525-1314.1996.00338.x.

Reddy, S.M., Kelley, S.P., Magennis, L., 1997. A microstructural and argon laserprobe study of shear zone development at the western margin of the Nanga Parbat-Haramosh Massif, western Himalaya. Contrib. Mineral. Petrol. 128, 16–29. https://doi.org/10.1007/s004100050290.

Reddy, S.M., Potts, G.J., Kelley, S.P., Arnaud, N.O., 1999. The effects of deformation-induced microstructures on intragrain 40Ar/39Ar ages in potassium feldspar. Geology 27, 363. https://doi.org/10.1130/0091-7613(1999)027<0363:TEODIM>2.3.CO;2.

Reddy, S.M., Potts, G.J., Kelley, S.P., 2001. 40Ar/39Ar ages in deformed potassium feldspar: evidence of microstructural control on Ar isotope systematics. Contrib. Mineral. Petrol. 141, 186–200. https://doi.org/10.1007/s004100000227.

Reddy, S.M., Collins, A.S., Buchan, C., Mruma, A.H., 2004. Heterogeneous excess argon and Neoproterozoic heating in the Usagaran Orogen, Tanzania, revealed by single grain 40Ar/39Ar thermochronology. J. Afr. Earth Sci. 39, 165–176. https://doi.org/10.1016/j.jafrearsci.2004.07.052.

Reddy, S.M., Timms, N.E., Pantleon, W., Trimby, P., 2007. Quantitative characterization of plastic deformation of zircon and geological implications. Contrib. Mineral. Petrol. 153, 625–645. https://doi.org/10.1007/s00410-006-0174-4.

Reddy, S.M., Timms, N.E., Hamilton, P.J., Smyth, H.R., 2009a. Deformation-related microstructures in magmatic zircon and implications for diffusion. Contrib. Mineral. Petrol. 157, 231–244. https://doi.org/10.1007/s00410-008-0331-z.

Reddy, S.M., Timms, N.E., Hamilton, P.J., Smyth, H.R., 2009b. Deformation-related microstructures in magmatic zircon and implications for diffusion. Contrib. Mineral. Petrol. 157, 231–244. https://doi.org/10.1007/s00410-008-0331-z.

Reddy, S.M., Saxey, D.W., Rickard, W.D.A., Fougerouse, D., Montalvo, S.D., Verberne, R., Riessen, A., 2020. Atom probe tomography: development and application to the geosciences. Geostand. Geoanal. Res. 44, 5–50. https://doi.org/10.1111/ggr.12313.

Renne, P.R., Mundil, R., Balco, G., Min, K., Ludwig, K.R., 2010. Joint determination of 40K decay constants and 40Ar*/40K for the Fish Canyon sanidine standard, and improved accuracy for 40Ar/39Ar geochronology. Geochem. Cosmochim. Acta 74, 5349–5367. https://doi.org/10.1016/j.gca.2010.06.017.

Ribeiro, B.V., Faleiros, F.M., Campanha, G.A.C., Lagoeiro, L., Weinberg, R.F., Hunter, N. J.R., 2019. Kinematics, deformational conditions and tectonic setting of the Taxaquara Shear Zone, a major transpressional zone of the Ribeira Belt (SE Brazil). Tectonophysics 751, 83–108. https://doi.org/10.1016/j.tecto.2018.12.025.

Ribeiro, B.V., Lagoeiro, L., Faleiros, F.M., Hunter, N.J.R., Queiroga, G., Raveggi, M., Cawood, P.A., Finch, M., Campanha, G.A.C., 2020a. Strain localization and fluid-assisted deformation in apatite and its influence on trace elements and U–Pb systematics. Earth Planet Sci. Lett. 545, 116421 https://doi.org/10.1016/j.epsl.2020.116421.

Ribeiro, B.V., Mulder, J.A., Faleiros, F.M., Kirkland, C.L., Cawood, P.A., O'Sullivan, G., Campanha, G.A.C., Finch, M.A., Weinberg, R.F., Nebel, O., 2020b. Using apatite to resolve the age and protoliths of mid-crustal shear zones: a case study from the Taxaquara Shear Zone, SE Brazil. Lithos 378–379, 105817. https://doi.org/10.1016/j.lithos.2020.105817.

Ribeiro, B.V., Faleiros, F.M., Campanha, G.A.C., Cawood, P.A., Kirkland, C.L., Barham, M., Martin, E.L., Seraine, M., Cabrita, D.I.G., Yogi, M.T.A.G., Almeida, V.V., Forero-Ortega, A.J.A., Dantas, E.L., 2022a. A Laurentian affinity for the Embu Terrane, Ribeira Belt (SE Brazil), revealed by zircon provenance statistical analysis. Geosci. Front., 101477 https://doi.org/10.1016/j.gsf.2022.101477.

Ribeiro, B.V., Finch, M.A., Cawood, P.A., Faleiros, F.M., Murphy, T.D., Simpson, A., Glorie, S., Tedeschi, M., Armit, R., Barrote, V.R., 2022b. From microanalysis to supercontinents: insights from the Rio apa terrane into the mesoproterozoic SW amazonian craton evolution during rodinia assembly. J. Metamorph. Geol. 40, 631–663. https://doi.org/10.1111/jmg.12641.

Ribeiro, B.V., Kirkland, C.L., Kelsey, D.E., Reddy, S.M., Hartnady, M.I.H., Faleiros, F.M., Rankenburg, K., Liebmann, J., Korhonen, F.J., Clark, C., 2023. Time-strain evolution of shear zones from petrographically constrained Rb–Sr muscovite analysis. Earth Planet Sci. Lett. 602, 117969 https://doi.org/10.1016/j.epsl.2022.117969.

Rogowitz, A., Huet, B., Schneider, D., Grasemann, B., 2015. Influence of high strain rate deformation on 40Ar/39Ar mica ages from marble mylonites (Syros, Greece). Lithosphere 7, 535–540. https://doi.org/10.1130/L455.1.

Rösel, D., Zack, T., 2022. LA-ICP-MS/MS single-spot Rb-Sr dating. Geostand. Geoanal. Res. https://doi.org/10.1111/ggr.12414.

Sanchez, G., Rolland, Y., Schneider, J., Corsini, M., Oliot, E., Goncalves, P., Verati, C., Lardeaux, J.M., Marquer, D., 2011. Dating low-temperature deformation by 40Ar/39Ar on white mica, insights from the Argentera-Mercantour Massif (SW Alps). Lithos 125, 521–536. https://doi.org/10.1016/j.lithos.2011.03.009.

Schmid, S.M., Casey, M., 1986. Analysis of some commonly observed quartz c-axis (A). In: Mineral and Rock Deformation: Laboratory Studies: the Paterson Volume. American Geophysical Union, Washington, D. C.

Schmitt, R.S., Trouw, R.A.J., Da Silva, E.A., de Jesus, J.V.M., da Costa, L.F.M., Passarelli, C.R., 2023. The Role of Crustal Scale Shear Zones in Southwest Gondwana Consolidation - Transatlantic Correlation. Geological Society, London. https://doi.org/10.1144/SP531-2022-278. Special Publications 531.

Schneider, S., Hammerschmidt, K., Rosenberg, C.L., 2013. Dating the longevity of ductile shear zones: insight from 40 Ar/39 Ar in situ analyses. Earth Planet Sci. Lett. 369–370, 43–58. https://doi.org/10.1016/j.epsl.2013.03.002.

Sheikh, H., Ebrahimi, R., Bagherpour, E., 2016. Crystal plasticity finite element modeling of crystallographic textures in simple shear extrusion (SSE) process. Mater. Des. 109, 289–299. https://doi.org/10.1016/j.matdes.2016.07.030.

Sherlock, S., Kelley, S., 2002. Excess argon evolution in HP–LT rocks: a UVLAMP study of phengite and K-free minerals, NW Turkey. Chem. Geol. 182, 619–636. https://doi.org/10.1016/S0009-2541(01)00345-X.

Steiger, R.H., Jager, E., 1977. Subcommission on geochronology: convention on the use of decay constants in geo-and cosmochronology. Earth Planet Sci. Lett. 36, 359–362.

Stipp, M., Stünitz, H., Heilbronner, R., Schmid, S.M., 2002. Dynamic Recrystallization of Quartz: Correlation between Natural and Experimental Conditions. Geological Society. Special Publications, London, pp. 171–190. https://doi.org/10.1144/GSL.SP.2001.200.01.11, 200.

ten Grotenhuis, S.M., Trouw, R.A.J., Passchier, C.W., 2003. Evolution of mica fish in mylonitic rocks. Tectonophysics 372, 1–21. https://doi.org/10.1016/S0040-1951(03)00231-2.

Tillberg, M., Drake, H., Zack, T., Kooijman, E., Whitehouse, M.J., Åström, M.E., 2020. In situ Rb-Sr dating of slickenfibres in deep crystalline basement faults. Sci. Rep. 10, 562. https://doi.org/10.1038/s41598-019-57262-5.

Timms, N.E., Kinny, P.D., Reddy, S.M., Evans, K., Clark, C., Healy, D., 2011. Relationship among titanium, rare earth elements, U-Pb ages and deformation microstructures in zircon: implications for Ti-in-zircon thermometry. Chem. Geol. 280, 33–46. https://doi.org/10.1016/j.chemgeo.2010.10.005.

Trouw, R.A.J., Passchier, C.W., Wiersma, D.J., 2010. Atlas of Mylonites and Related Microstructures. Springer.

Van Daele, J., Dewaele, S., Melcher, F., Onuk, P., Spikings, R., Glorie, S., Jepson, G., Muchez, P., 2020. Geochronology of metamorphism, deformation and fluid circulation: a comparison between and Ar-Ar phyllosilicate and U-Pb apatite systematics in the Karagwe-Ankole Belt (Central Africa). Gondwana Res. 83, 279–297. https://doi.org/10.1016/j.gr.2020.02.008.

Verberne, R., Reddy, S.M., Saxey, D.W., Fougerouse, D., Rickard, W.D.A., Quadir, Z., Evans, N.J., Clark, C., 2022. Dislocations in minerals: fast-diffusion pathways or trace-element traps? Earth Planet Sci. Lett. 584, 117517 https://doi.org/10.1016/j.epsl.2022.117517.

Vermeesch, P., 2018. IsoplotR: a free and open toolbox for geochronology. Geosci. Front. 9, 1479–1493. https://doi.org/10.1016/j.gsf.2018.04.001.

Viegas, G., Menegon, L., Archanjo, C., 2016. Brittle grain-size reduction of feldspar, phase mixing and strain localization in granitoids at mid-crustal conditions (Pernambuco shear zone, NE Brazil). Solid Earth 7, 375–396. https://doi.org/10.5194/se-7-375-2016.

Villa, I.M., De Bièvre, P., Holden, N.E., Renne, P.R., 2015. IUPAC-IUGS recommendation on the half life of 87Rb. Geochem. Cosmochim. Acta 164, 382–385. https://doi.org/10.1016/j.gca.2015.05.025.

Von Blanckenburg, F., Villa, I.M., Baur, H., Morteani, G., Steiger, R.H., 1989. Time calibration of a PT-path from the western tauern window, eastern Alps: the problem of closure temperatures. Contrib. Mineral. Petrol. 101, 1–11. https://doi.org/10.1007/BF00387196.

Warren, C.J., Hanke, F., Kelley, S.P., 2012. When can muscovite 40Ar/39Ar dating constrain the timing of metamorphic exhumation? Chem. Geol. 291, 79–86. https://doi.org/10.1016/j.chemgeo.2011.09.017.

Wawrzenitz, N., Krohe, A., Rhede, D., Romer, R.L., 2012. Dating rock deformation with monazite: the impact of dissolution precipitation creep. Lithos 134 (135), 52–74. https://doi.org/10.1016/j.lithos.2011.11.025.

White, S.H., Burrows, S.E., Carreras, J., Shaw, N.D., Humphreys, F.J., 1980. On mylonites in ductile shear zones. J. Struct. Geol. 2, 175–187. https://doi.org/10.1016/0191-8141(80)90048-6.

Whitney, D.L., Evans, B.W., 2010. Abbreviations for names of rock-forming minerals. Am. Mineral. 95, 185–187. https://doi.org/10.2138/am.2010.3371.

Williams, M.L., Jercinovic, M.J., Harlov, D.E., Budzyń, B., Hetherington, C.J., 2011. Resetting monazite ages during fluid-related alteration. Chem. Geol. 283, 218–225. https://doi.org/10.1016/j.chemgeo.2011.01.019.

Wilson, C.J.L., Bell, I.A., 1979. Deformation of biotite and muscovite: optical microstructure. Tectonophysics 58, 179–200. https://doi.org/10.1016/0040-1951(79)90328-7.

Wölfler, A., Kurz, W., Danišík, M., Rabitsch, R., 2010. Dating of Fault Zone Activity by Apatite Fission Track and Apatite (U-Th)/He Thermochronometry: a Case Study from the Lavanttal Fault System (Eastern Alps). https://doi.org/10.1111/j.1365-3121.2010.00943.x. Terra Nova no-no.

Woodhead, J.D., Hergt, J.M., 2001. Strontium, neodymium and lead isotope analyses of NIST glass certified reference materials: srm 610, 612, 614. Geostand. Geoanal. Res. 25, 261–266. https://doi.org/10.1111/j.1751-908X.2001.tb00601.x.

Wright, S.I., Suzuki, S., Nowell, M.M., 2016. In situ EBSD observations of the evolution in crystallographic orientation with deformation. J. Occup. Med. 68, 2730–2736. https://doi.org/10.1007/s11837-016-2084-x.

Zack, T., Hogmalm, K.J., 2016. Laser ablation Rb/Sr dating by online chemical separation of Rb and Sr in an oxygen-filled reaction cell. Chem. Geol. 437, 120–133. https://doi.org/10.1016/j.chemgeo.2016.05.027.

Zametzer, A., Kirkland, C.L., Barham, M., Hartnady, M.I.H., Bath, A.B., Rankenburg, K., 2022. Episodic alteration within a gold-bearing Archean shear zone revealed by in situ biotite Rb–Sr dating. Precambrian Res. 382, 106872 https://doi.org/10.1016/j.precamres.2022.106872.

Zhu, G., Wang, Y., Liu, G., Niu, M., Xie, C., Li, C., 2005. 40Ar/39Ar dating of strike-slip motion on the Tan-Lu fault zone, East China. J. Struct. Geol. 27, 1379–1398. https://doi.org/10.1016/j.jsg.2005.04.007.